Implementation and calibration of a mesoscale model for amorphous plasticity based on shear transformation dynamics

Frederik Van Loock[a,*], Laurence Brassart[b] and Thomas Pardoen[a]

[a] Institute of Mechanics, Materials & Civil Engineering, UCLouvain, Place Sainte-Barbe 2, 1348 Louvain-la-Neuve, Belgium,
frederik.vanloock@uclouvain.be, thomas.pardoen@uclouvain.be

[b] Department of Engineering Science, Parks Road, Oxford OX1 3PJ, United Kingdom
laurence.brassart@eng.ox.ac.uk

*corresponding author

Keywords: Shear transformation zone (STZ), B. Glass material, B. Polymeric material, C. Elastic-plastic material, D. Finite elements

Highlights

- Prediction of plasticity in amorphous solids via a shear transformation zone (STZ) model
- Mesoscale formalism implemented in an FE programme; code is made available
- Calculations for both a model metallic and a polymeric glass in compression
- A mean-field approximation for the predicted yield strength
- Guidelines for model calibration and time control via the mean-field estimation

Abstract

A mesoscale numerical model based on shear transformation zone (STZ) theory is implemented in a commercial finite element software. The model is designed to predict the (visco)plastic deformation response of amorphous solids at the nano- and micro-scale. The theoretical framework relies on earlier models developed by Bulatov and Argon (1994a) and of Homer and Schuh (2009). We justify the potential of the computational model by conducting reference calculations for model metallic and polymeric glasses in plane strain compression. Emphasis is placed on the effect of time and space discretisation on the predicted macroscopic response. The dependence of the predicted yield strength upon the values of the fundamental model parameters is analysed via a mean-field approximation. The mean-field approximation is validated based on a series of simulations in model parameter space. We provide guidelines for a straightforward but consistent parameter identification method via the mean-field approximation while starting from experimental data.

1. Introduction

There is a growing interest in the use of shear transformation zone (STZ) dynamics to model the inelastic response of amorphous materials at the mesoscale (Tanguy, 2021). Shear transformation theory was originally developed by Argon and co-workers (Argon, 1979; Argon and Kuo, 1979; Argon and Shi, 1983) to describe the viscoplastic behaviour of metallic glasses. According to STZ theory, the inelastic deformation of metallic glasses at a temperature T below the glass transition temperature T_g is governed by the local, thermally activated and permanent distortion of small material volumes (on the order of 10 to 100 atoms) (Xu et al., 2018). The local distortion is mainly driven by shear, resulting in a local shear transformation, possibly involving a transient dilatation contribution (Boioli et al., 2017; Lu et al., 2018; Pan et al., 2011). The attempt rate of individual STZs to deform follows transition state theory, where the energy barrier for STZ transformation is estimated by considering the uniform deformation of the transforming material volume within the elastic matrix as an Eshelby inclusion problem (Argon, 1979; Eshelby, 1957). Distortion of the local stress field in the surrounding matrix upon the activation of an STZ increases the probability for a neighbouring STZ to transform. The resulting avalanche of sessile STZ activations can lead to the localisation of flow in the form of (critical) shear bands (Chen and Lin, 2010; Chen et al., 2013; Gan et al., 2019; Kosiba et al., 2019; Perepezko et al., 2014; Wang et al., 2015).

There is extensive numerical (Argon, 2013; Avila et al., 2019; Boioli et al., 2017; Hu et al., 2016; Xu et al., 2018) and some indirect experimental (Albaret et al., 2016; Argon and Kuo, 1979; Pan et al., 2008; Wu et al., 2015) evidence for the large strain, viscoplastic deformation behaviour of metallic glasses at $T/T_g < 1$ to be dictated by STZ dynamics. In addition, the STZ theory has been used to analyse the viscoplastic deformation behaviour of a wider range of amorphous materials such as polymeric glasses (Chevalier et al., 2018; Malekmotiei et al., 2015; Voyiadjis et al., 2018; Voyiadjis and Samadi-Dooki, 2016) and non-crystalline oxides (Argon, 2013; Urata and Li, 2018). The macromolecular nature of polymers involves specific permanent changes of configurations to which a fictitious operating volume is associated to fit with the STZ paradigm (Argon, 2013; Fujimoto et al., 2019; Hossain et al., 2010; Jatin et al., 2014; Sundararaghavan and Kumar, 2013; Voyiadjis et al., 2014).

Atomistic models have been used to study the fundamental properties of STZs; these include the shape and size of the STZs and the conditions for STZ activation and their relation with pre-existing

microstructure (Derlet and Maaß, 2021, 2018; Ding et al., 2021; Kosiba et al., 2019; Martinet et al., 2020). However, due to their high demand in computational power, they are restricted to domain sizes below those required to resolve critical shear band formation in bulk and confined amorphous solids at realistic deformation rates (Gartner and Jayaraman, 2019; Jafary-Zadeh et al., 2016; Kosiba et al., 2019; Park et al., 2018; Zhong et al., 2016a; Zhou et al., 2013). A vast amount of continuum models are available to predict the deformation behaviour of glassy solids at larger length scales. Anand and co-workers developed several constitutive models to predict the large deformation response of metallic (Anand and Su, 2007, 2005) and polymeric (Ames et al., 2009; Anand et al., 2009; Srivastava et al., 2010) glasses. These sophisticated thermo-mechanical models give excellent fits to measured uniaxial stress-strain data for a wide range of strain rates and temperatures (below to just above T_g), and include the prediction of complex deformation phenomena such as post-yield strain softening, the Bauschinger effect, and non-linear unloading. More recent contributions extended the formulation of constitutive continuum models for glassy and semi-crystalline polymers by focusing on, for instance, damage and fracture (Krairi and Doghri, 2014; Narayan and Anand, 2021), degree of crystallinity (Ayoub et al., 2011; Felder et al., 2020; Hachour et al., 2014; Regrain et al., 2009), non-isothermal loading and self-heating (Johnsen et al., 2019; Krairi et al., 2019), non-monotonic and cyclic loading (Barriere et al., 2020; Federico et al., 2020; Khan and Yeakle, 2011; Shojaei and Volgers, 2017), shape memory effects (Baghani et al., 2012; Shojaei and Guoqiang L., 2014), and stress relaxation/strain recovery subsequent to large deformation (Huang et al., 2011; Wang et al., 2019).

Continuum approaches typically rely on a large number of (mostly phenomenological) model parameters, and, more importantly, they do not capture the discrete shear transformation events and the resulting heterogeneous nature of the stress and strain field of the deformed amorphous solid. This requires a numerical (mesoscale) approach which explicitly accounts for multiple STZs interacting through the elastic stress field. Mesoscale constitutive models relying on STZ dynamics can fill the gap in spatial and temporal resolution between the continuum and atomistic approaches. Simulations conducted with mesoscale STZ models shed light on the role of processing conditions on the large deformation response of amorphous solids with only a few physical fitting parameters (Chevalier et al., 2018; Hardin and Homer, 2015; Homer and Schuh, 2009; Kondori et al., 2018; Wang et al., 2018; Zhao et al., 2013). These models also provide insight into the cooperation between individually activated STZs leading to the formation of critical shear bands and material

failure (Harris et al., 2016; Tong et al., 2016; Wu et al., 2015). Hence, they can be used to predict the ductility of bulk amorphous solids and related size effects (Dong et al., 2021; Jang et al., 2011; Yoo et al., 2012). In addition, they can be used to analyse the ductility of hybrid material systems comprising an amorphous phase (Choi et al., 2012; Rozanski and Galeski, 2013; Sun et al., 2016; Zhou et al., 2013). Excellent examples of such hybrid material concepts include (1) fibre-reinforced polymer composites and thin adhesive joints where the evolution of plasticity in the glassy polymer matrix or adhesive is sensitive to the degree of confinement (Lopes Fernandes et al., 2019; Pardoen et al., 2021, 2005; Van Loock et al., 2019), and (2) metallic glass-based composites where the interaction of dislocations and STZ transformations at the interfaces between the crystalline and amorphous metallic phases may lead to an enhanced macroscopic ductility (Donohue et al., 2007; Hardin and Homer, 2015; Jiang et al., 2021; Phan et al., 2020; Sun et al., 2018; Wang et al., 2015; Zhao et al., 2021; Zhou et al., 2013).

The first STZ-based numerical constitutive model was developed by Bulatov and Argon (1994a), who discretised a two-dimensional (2D) linear, elastic solid with equisized hexagonal lattice elements. Each lattice element is considered as an STZ; the selection of the STZ to activate (and the corresponding value of the time increment during which the distortion takes place) is dictated by a rejection-free kinetic Monte Carlo (KMC) algorithm (Bortz et al., 1975). The activated STZ is subjected to a uniform pure shear eigenstrain and the resulting equilibrium stress field in the deformed solid is calculated via pre-tabulated lattice Green tensor data. The seminal model of Bulatov and Argon (1994a) predicts the characteristic transition of metallic glasses from quasi-homogeneous deformation behaviour at T close to T_g, to localised flow at lower temperatures. In addition, the model provides insights into the equilibrium and relaxational properties of amorphous solids (Bulatov and Argon, 1994b) and the role of structural disorder on the degree of intrinsic post-yield softening (Bulatov and Argon, 1994c).

Inspired by the work of Argon and Bulatov, Homer and Schuh (2009) developed the first 2D numerical model relying on finite element (FE) calculations to obtain the equilibrium stress field in an STZ-enriched model material. The model of Homer and Schuh was further refined by incorporating a free volume state parameter (Chen et al., 2011; Jiang et al., 2021; Li et al., 2013; Voyiadjis and Samadi-Dooki, 2016) and extending the plane strain 2D model to three dimensions (Homer and Schuh, 2010). They also investigated more complicated geometries and loading cases

such as the cyclic indentation of bulk metallic glasses (Packard et al., 2010) and the role of crystalline inclusions on the (de-)localisation of flow in a metallic glass (Hardin and Homer, 2015). Other studies with the FE-based mesoscale model of Homer and Schuh examined the effect of the macroscopic stress state and the temperature on the correlation behaviour of STZ activations (Homer et al., 2010), and the dependence of shear band nucleation and propagation rate upon strain rate (Harris et al., 2016). Wang et al. (2018) combined molecular dynamics simulations with mesoscale calculations based on the model of Homer and Schuh to analyse the sensitivity of shear band formation to the correlation length of the initial elastic material heterogeneity in metallic glasses. Recent work by Hardin (2019) improved the numerical efficiency of Homer and Schuh's model to simulate three dimensional domain sizes accessible via micromechanical tests.

The model of Homer and Schuh assigns homogeneous properties to the STZ events. However, atomistic calculations suggest that key properties of the STZ transformation events (i.e. the magnitude of the shear eigenstrain upon STZ activation, γ_0, and the STZ activation volume, v_0) are heterogeneously distributed in an amorphous solid (Albaret et al., 2016; Zhong et al., 2016b). The atomistic simulations of Albaret and co-workers indicate that inelastic events in metallic glasses can be described via exponentially decaying distribution functions of γ_0 and v_0 (Albaret et al., 2016; Boioli et al., 2017), justifying the use of a constant value of γ_0 and v_0 in Homer and Schuh's model. Zhao and co-workers explored the effect of heterogenous STZ properties and modified the model of Homer and Schuh by introducing random heterogeneous transformation modes and strain-induced softening to study shear band formation during straining of a metallic glass (Zhao et al., 2013).

Alternative approaches for numerical STZ-enriched mesoscale models also exist. In contrast to the models of Bulatov and Argon (1994a), and Homer and Schuh (2009), which combine transition state theory and the KMC method to dictate the STZ dynamics, they typically use a less sophisticated stress- or energy-based criteria for STZ activation (Budrikis et al., 2017; Budrikis and Zapperi, 2013; Sandfeld et al., 2015). A recent computationally efficient numerical model was developed by Kondori and co-workers (Kondori et al., 2018, 2016; Vasoya et al., 2021, 2020). This model solves boundary value problems with an STZ-enriched solid by superposing the analytical expressions for individual STZ transition in an infinite linear, elastic solid with an FE-generated solution of the corresponding image field satisfying the boundary conditions.

Mesoscale numerical models relying on STZ dynamics are useful to predict and analyse the large strain deformation behaviour of a wide range of amorphous solids at the mesoscale. Yet, some outstanding questions remain. Many of these are related to the basic constitutive assumptions of the framework and include, for instance, the dependence of the value of the STZ activation volume v_0 upon temperature and the evolution laws of a free volume-like state parameter (Albaret et al., 2016; Jiang et al., 2021; Richard et al., 2020; Xu et al., 2018). These issues are obscured by the fact that, despite the strong evidence for STZ dynamics provided by atomistic simulations and by indirect measurements conducted in analogous, larger scale material systems, no direct observations of STZ-like inelastic events in metallic or polymeric glasses have been reported so far (Falk and Langer, 2011; Im et al., 2018; Jensen et al., 2014; Lu et al., 2018).

From a more practical point of view, the selection of the values of the STZ model parameters based on measurement data remains a somewhat arbitrary curve fitting task to date (Chevalier et al., 2018; Homer et al., 2010; Homer and Schuh, 2009; Pardoen et al., 2021; Wang et al., 2018). An analysis on the sensitivity of the mesoscale STZ model's response to the values of its basic ingredients is essential to guide the parameter identification process, but has not been explored in detail so far. Calibration of STZ models in the literature is typically guided by atomistic simulations (to provide a physical range for the value of γ_0) and uniaxial tensile or compression tests on macro-sized samples and/or (nano)indentation tests on small material volumes (to provide a range for the value of v_0). In addition, recent work of Vasoya and co-workers (2020, 2019) identified theoretical limits for the value of γ_0 to prevent negative dissipation rate in a purely mechanistic mesoscale framework (Kondori et al., 2018, 2016). However, computed magnitudes of the transformation eigenstrain via atomistic simulations sometimes exceed those limit values (Albaret et al., 2016; Boioli et al., 2017; Zhong et al., 2016b).

Scope of study

This study aims to contribute to the development and consolidation of discrete mesoscale STZ models by proposing a robust numerical implementation within a commercial finite element software and by addressing some remaining open questions. These questions include:

- The effect of the time-stepping scheme and domain size effects;

- The role of key model parameters (transformation strain, γ_0, and activation volume, v_0) on the predicted macroscopic response;
- The identification of these parameters based on an amorphous solid's measured macroscopic response.

To this end, we consider a revised and simplified theoretical framework of the mesoscale models developed by Bulatov and Argon (1994a) and Homer and Schuh (2009). We limit our attention to 2D plane strain compression of a rectangular domain with periodic boundary conditions. We implemented the discrete model in the Abaqus FE software package (Dassault Systèmes Simulia Corp, 2017), and publish the code including the developed user-defined material routine (UMAT) in the Supplementary Information (SI). It is hoped that the publication of the code will facilitate future development of numerical constitutive models relying on STZ dynamics. We further propose an analytical mean-field approximation of the discrete model which is useful for parametric studies and model calibration. Computational results and mean-field predictions are analysed via reference calculations for a model metallic glass and a model polymeric glass. We also examine the dependence of the predicted yield strength upon the selected combination of model parameters. Calibration maps are constructed via the mean-field approximation to guide the parameter identification of the STZ model based on measured data.

2. Theory

A simplified version of the numerical model of Homer and Schuh (2009) is implemented, based on the original formulation of the mesoscale framework developed by Bulatov and Argon (1994a). We chose to focus on this relatively straightforward version without, for instance, introducing a free volume state parameter (Li et al., 2013), as we aim to shed light on the dependence of the predicted deformation response of the STZ-enriched solid upon the value of the model's main parameters.

2.1. Attempt rate estimate

Consider a homogeneous and isotropic linear, elastic solid with shear modulus G and Poisson's ratio ν. We define n spherical[1], equisized material domains of volume Ω which can deform inelastically and uniformly in pure shear (with an engineering shear strain of magnitude γ_0). The probability per unit time for the i-th STZ (i = 1, 2, …, n) to be activated, $\dot{s}_i$, follows the transition state theory (Argon, 1979; Kocks et al., 1975):

$$\dot{s}_i = f_\mathrm{d} \exp\left[-\frac{\Delta G_i}{k_\mathrm{B} T}\right], \tag{1}$$

where f_d (= 10^{12} s^{-1}) is a reference attempt frequency on the order of the solid's Debye frequency (Argon, 2013), k_B is Boltzmann's constant, and ΔG_i the free enthalpy equal to the change in Helmholtz free energy, ΔF, minus the available work:

$$\Delta G_i = \Delta F - 0.5 \nu_0 \bar{\tau}_{\mathrm{max},i}, \tag{2}$$

where $\bar{\tau}_{\mathrm{max},i}$ is the maximum value of the resolved shear stress for the STZ's averaged stress state $\bar{\boldsymbol{\sigma}}_i$ and ν_0 is the so-called (apparent) activation volume v_0. Note that we adopt the standard definition of the activation volume such that work done during the deformation of an STZ by a stress $\bar{\tau}_{\mathrm{max},i}$ is proportional to the undeformed STZ volume times the applied shear eigenstrain: v_0

[1] We follow Argon's theory who idealised the individual STZs as spheres to calculate the energy barrier for STZ activation via Eshelby's solution for an unstressed solid comprising a spherical material domain subjected to a pure shear eigenstrain. Recent molecular dynamics calculations support this idealisation (Tanguy, 2021).

= $\Omega\gamma_0$. The value of the stress-independent energy barrier ΔF is based on Argon's approach (Argon, 1979; Argon and Shi, 1983). The change in Helmholtz free energy comprises three terms:

$$\Delta F = \Delta F_1 + \Delta F_2 + \Delta F_3, \tag{3}$$

where ΔF_1 is the transformation shear strain energy of the constrained STZ, ΔF_2 is the associated temporary dilation strain energy, and ΔF_3 is the inter-atomic (or inter-molecular) potential energy for unconstrained deformation. The first two terms are calculated using Eshelby's solution for an isolated transforming inclusion (Eshelby, 1957), and are given by:

$$\Delta F_1 = \frac{7-5\nu}{30(1-\nu)} G\gamma_0 v_0, \tag{4}$$

and

$$\Delta F_2 = \beta^2 \frac{2(1+\nu)}{9(1-\nu)} G\gamma_0 v_0, \tag{5}$$

respectively. In Eq. (5), β is a dilatancy factor equal to the ratio of the *unconstrained* temporary dilation strain to the *unconstrained* shear transformation strain, γ_0 (Argon, 2013). We follow the approach of Argon and Shi (1983, 1982) and assume the ratio of the *constrained* temporary dilation strain to the *constrained* shear transformation strain to be equal to unity. Hence, β reads (Argon and Shi, 1983):

$$\beta = \frac{6}{15}\frac{(4-5\nu)}{(1+\nu)}, \tag{6}$$

The value of ΔF_3 is calculated via (Argon and Shi, 1983):

$$\Delta F_3 = \frac{v_0 \hat{\tau}}{2}. \tag{7}$$

where $\hat{\tau}$ is a threshold strength close to the athermal shear strength of the solid. Now, upon making use of Eqs. (3) to (7), we may write:

$$\Delta F = v_0 \left[CG\gamma_0 + 0.5\hat{\tau} \right], \tag{8}$$

where *C* is defined as:

$$C = \frac{7-5\nu}{30(1-\nu)} + \frac{8(4-5\nu)^2}{225(1-\nu^2)}. \tag{9}$$

Hence, Eq. (1) may be re-written in the form:

$$\dot{s}_i = f_{\mathrm{d}} \exp\left[\frac{-v_0}{k_{\mathrm{B}}T}\left(CG\gamma_0 + 0.5\left(\hat{\tau} - \bar{\tau}_{\max,i}\right)\right)\right], \tag{10}$$

upon insertion of Eqs. (2) and (8) into Eq. (1)

2.2 The KMC algorithm

The simulation starts at time t = 0. The simulation residence time Δt_j is defined as the time increment between two STZ transformations. The simulation time at the beginning of a new increment is simply updated via:

$$t_{j+1} = t_j + \Delta t_j. \tag{11}$$

The KMC algorithm dictates the value of the time increment Δt_j at $t = t_j$ and selects the STZ to transform during this time increment. A brief justification of the residence time calculation procedure is as follows (a more detailed derivation can be found in the work of Gillespie (1976)). We assume that the value of $\dot{s}_i$ calculated via Eq. (10) for each STZ depends on the solution of the boundary value problem at the end of the previous increment only (i.e. independent of solutions at previous increments) and that it remains constant during the residence time period. The STZ events can then be idealised as a series of Poisson processes, where the escape or transition time of the *i*-th STZ at $t = t_j$ follows an exponential probability distribution function $p_{i,j}(t)$:

$$p_{i,j}(t) = \dot{s}_{i,j} \exp\left(-\dot{s}_{i,j} t\right), \tag{12}$$

where $\dot{s}_{i,j}$ is the calculated attempt rate of the *i*-th STZ at $t = t_j$ via Eq. (10). The distribution function $p_{\mathrm{tot}}(t)$ of the first transition time of the entire system composed of *n* STZs reads:

$$p_{\mathrm{tot},j}(t) = \dot{s}_{\mathrm{tot},j} \exp(-\dot{s}_{\mathrm{tot},j} t), \tag{13}$$

where the total attempt rate $\dot{s}_{\mathrm{tot},j}$ is defined as:

$$\dot{s}_{\mathrm{tot},j} = \sum_{i=1}^{n} \dot{s}_{i,j} \,. \tag{14}$$

The cumulative distribution function $P_{\mathrm{tot},j}(t)$ of the first transition time of the system is obtained by integration of Eq. (13):

$$P_{\mathrm{tot},j}(t) = 1 - \exp\left(-\dot{s}_{\mathrm{tot},j} t\right). \tag{15}$$

The collection of residence times in the simulation needs to follow this distribution. We therefore make use of a standard Monte Carlo procedure and draw a uniformly distributed random number ξ_1 within the interval]0,1]. Inverting Eq. (15) gives the residence time at $t = t_j$:

$$\Delta t_j = \frac{-\ln(1-\xi_1)}{\dot{s}_{\mathrm{tot},j}} \,. \tag{16}$$

The expected value of $\ln(1-\xi_1)$ is equal to the expected value of $\ln(\xi_1)$ for the uniformly distributed random number ξ_1 on]0,1]. Hence, the time increment is calculated via:

$$\Delta t_j = \frac{-\ln(\xi_1)}{\dot{s}_{\mathrm{tot},j}} \,. \tag{17}$$

The choice of the STZ to activate during this time increment is biased by the relative values of the attempt rates of the individual STZs at $t = t_j$. We make use of a rejection-free procedure following the '*n*-fold' method of Bortz and co-workers (Bortz et al., 1975): a second uniformly distributed random number ξ_2 is drawn within the interval]0,1] and select the *i*-th STZ to transform at $t = t_j + \Delta t_j$ satisfying the condition:

$$\sum_{1}^{i-1} \dot{s}_{i,j} < \xi_2 \dot{s}_{\mathrm{tot},j} \le \sum_{1}^{i} \dot{s}_{i,j} \,. \tag{18}$$

3. Model implementation

The theoretical framework detailed in section 2 is implemented in 2D (plane strain) in the Abaqus FE software package via user-defined routines, including a user-defined material routine (UMAT). The FE calculations are required to calculate the equilibrium stresses and strains in the solid upon each STZ activation event and to inform the KMC algorithm with the individual attempt rate of the STZs for the next STZ event. A summary of the calculation steps followed by the framework is given at the end of this section.

3.1 Discretisation and STZ definition

A 2D solid is discretised into plane strain, second-order triangular elements (CPE6) of approximately equal areas. Each element gives rise to one STZ. An STZ comprises this central element and its neighbouring (node-sharing) elements. Hence, the number of STZs n is equal to the number of elements discretising the STZ-enriched solid and one element can be part of multiple STZs, see Fig. 1a. The assumption of overlapping STZs corresponds to the idea of a group of atoms or molecules in the amorphous solid which may participate in separate STZ events with different atoms or molecules. When periodic boundary conditions are used on a regular (e.g. rectangular) domain, STZs with a central element comprising a node on the domain's boundary also contain elements at the opposing boundary as illustrated in Fig. 1a.

Finite element meshes were produced using the standard irregular meshing algorithm of Abaqus on rectangular simulation domains. When the number of elements along the smallest dimension is sufficiently high (i.e. above 10), the average number of elements per STZ, n_{el}, is about 12.2. This value is close to the one selected by Homer and Schuh, who found that the choice $n_{\mathrm{el}} = 13$ is sufficient for the Eshelby solution to apply to the case of a single FE-discretised STZ in an infinite medium and subjected to a uniform shear strain (Homer and Schuh, 2009). However, it is emphasised that the computed deformation response also depends on the number of STZs discretising the simulated domain, and hence also on the total number of finite elements in the discretisation. Since a set length scale is implicitly attributed to each STZ (via its activation volume), increasing the number of STZs in the simulation domain amounts to increasing the domain length as well. Domain size effects are explored later in this paper.

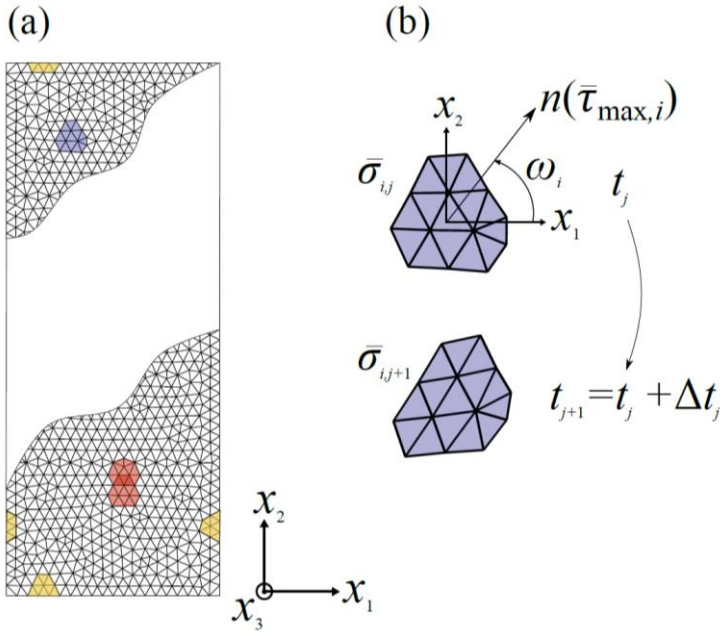

Fig. 1: (a) Illustration of a partially meshed, rectangular STZ-enriched material domain with an arbitrarily highlighted single STZ (blue), a pair of overlapping STZs (red), and two STZs with elements on opposing boundaries to satisfy periodic boundary conditions (yellow). (b) At the start of the simulation increment, $t = t_j$, a STZ is randomly selected by the KMC algorithm and its average stress state $\bar{\boldsymbol{\sigma}}_i$ is calculated. The angle indicates the maximum shear direction $n(\bar{\tau}_{\max,i})$, i.e. the direction normal to the plane experiencing the maximum in-plane shear stress of magnitude $\bar{\tau}_{\max,i}$. At $t = t_{j+1}$, the selected STZ is subjected to a uniform, pure shear eigenstrain of magnitude γ_0 in the direction of $n(\bar{\tau}_{\max,i})$.

3.2 The shear transformation event

One and only one STZ is selected to deform per time increment via the KMC algorithm detailed above. All elements of this activated STZ are subjected to a uniform eigenstrain in the direction of the maximum in-plane shear stress[2], $\bar{\tau}_{\max,i}$. To illustrate this principle for the plane strain solid, consider an arbitrarily selected STZ *i* with average stress state $\bar{\boldsymbol{\sigma}}_i = \{\bar{\sigma}^i_{11}, \bar{\sigma}^i_{22}, \bar{\sigma}^i_{33}, \bar{\sigma}^i_{12}\}$ in the global coordinate system at the start of an increment, see Fig. 1b. Here, the average stress is calculated by volume averaging of the stress at the integration points of the elements belonging to the STZ. The corresponding in-plane principal stresses $\bar{\sigma}^i_{\mathrm{I}}$ and $\bar{\sigma}^i_{\mathrm{II}}$ (where $\bar{\sigma}^i_{\mathrm{I}} > \bar{\sigma}^i_{\mathrm{II}}$) read:

$$\bar{\sigma}^i_{\mathrm{I,II}} = \frac{\bar{\sigma}^i_{11} + \bar{\sigma}^i_{22}}{2} \pm \left(\left(\frac{\bar{\sigma}^i_{11} - \bar{\sigma}^i_{22}}{2} \right)^2 + \left(\bar{\sigma}^i_{12} \right)^2 \right)^{\frac{1}{2}}, \tag{19}$$

and the value of $\bar{\tau}_{\max,\,i}$ reads:

$$\bar{\tau}_{\max,\,i} = \frac{\bar{\sigma}^i_{\mathrm{I}} - \bar{\sigma}^i_{\mathrm{II}}}{2}. \tag{20}$$

The corresponding maximum shear direction is found via standard Mohr circle analysis:

$$\omega_i = \frac{1}{2} \tan^{-1} \left(\frac{2\bar{\sigma}^i_{12}}{\bar{\sigma}^i_{11} - \bar{\sigma}^i_{22}} \right) - \frac{\pi}{4}. \tag{21}$$

When an STZ *i* is activated, its constitutive elements are subjected to a pure (engineering) shear eigenstrain of magnitude γ_0 in the direction of $\bar{\tau}_{\max,\,i}$. The resolved components of the applied true eigenstrain increments $\Delta\epsilon_{ij}$ with respect to the global coordinate system read:

$$\Delta\epsilon_{11} = \frac{-\gamma_0}{2} \sin\left(2\omega_i\right) \tag{22}$$

$$\Delta\epsilon_{22} = \frac{\gamma_0}{2} \sin\left(2\omega_i\right)$$

[2] The *j* increment subscript is omitted for convenience in this section.

$$\Delta\epsilon_{12} = \frac{\gamma_0}{2}\cos\left(2\omega_i\right) \ .$$

The equilibrium stress state of the deformed solid upon an STZ activation is calculated via the constitutive relation:

$$\boldsymbol{\sigma} = \mathbf{C} : \left(\boldsymbol{\varepsilon} - \boldsymbol{\epsilon}\right) \tag{23}$$

where $\mathbf{C}$ is the isotropic elastic stiffness tensor (specified in the following through the shear modulus and Poisson's ratio), $\boldsymbol{\varepsilon}$ the total strain, and $\boldsymbol{\epsilon}$ the accumulated inelastic, transformation strain: $\boldsymbol{\epsilon} = \sum \Delta\boldsymbol{\epsilon}$, where the summation extends over all past time increments.

3.3 Time step selection

One important feature of the numerical procedure is that the value of every time increment is prescribed by the KMC algorithm and depends on the average stresses in the STZs at the beginning of the increment. This also applies to the first simulation time step, prior any STZ activation. However, we found that the initial time step value calculated from the KMC procedure can be too large and lead to unphysical results. In the following, we discuss a procedure to regulate the time increment in a robust manner. The procedure involves the definition of a maximum, critical value of the time increment, Δt_{crit}.

As an illustration, consider an initial homogeneous stress distribution equal to zero (i.e. $\bar{\boldsymbol{\sigma}}$ = 0 for all STZs at t = 0). The initial value of the maximum in-plane shear stress $\bar{\tau}_{\max}$ is equal to 0 for all STZs. Making use of Eq. (10), the value the initial attempt rate $\dot{s}_0$ of the STZs reads:

$$\dot{s}_0 = f_{\text{d}} \exp\left[\frac{-v_0}{k_{\text{B}}T}\left(CG\gamma_0 + 0.5\hat{\tau}\right)\right], \tag{24}$$

and the value of Δt_0 is determined via Eq. (17):

$$\Delta t_0 = \frac{-\ln\left(\xi_1\right)}{n\dot{s}_0} \ . \tag{25}$$

Note that there is no STZ activation during the first increment. In general, the value of $\dot{s}_0$ calculated from Eq. (17) is low, as a direct consequence of the initial stress field. As a result, the initiation

time step can be large and approaches the time to reach (macroscopic) yielding. Excessively large initial time increments must be avoided as they can unphysically delay the series of STZ activations dictating the onset of the macroscopic plastic response of the material. A typical example is an artificial overshoot of the flow strength in a simple compression or tensile test; an illustration of this behaviour is shown later in this paper.

To prevent this unphysical response, we adopt the following pragmatic approach and constrain the initial time step not to exceed a maximum, critical value, Δt_{crit} . A similar strategy was followed by Packard and et al. (2010) and Homer et al. (2014) to regulate the evolution of the time steps in simulations with the mesoscale STZ model of Homer and Schuh (2009). However, they did not provide a justification for the selected value of Δt_{crit} . Here, we propose a straightforward rationale for the choice of Δt_{crit} when calibrating the framework to data of a standard tensile or compression tests (with a controlled macroscopic strain rate $\dot{\varepsilon}_{\text{t}}$ and testing temperature T_{t}) on an amorphous solid of interest. We define Δt_{crit} as a fraction of the loading time needed to reach the material's yield strain:

$$\Delta t_{\text{crit}} = \frac{\alpha(1-\nu)\sigma_y}{2G\dot{\varepsilon}_{\text{t}}}, \tag{26}$$

where σ_y is the yield strength for $\dot{\varepsilon} = \dot{\varepsilon}_{\text{t}}$ and $T = T_{\text{t}}$ and α is a constant lower than unity. We have used $\alpha = 0.1$ for all numerical predictions in this work. For a successful implementation of the time increment bound via Eq. (26), it is convenient to estimate, a priori, the value of the predicted yield strength by the framework as a function of the selected values of the model parameters. A mean-field approximation, useful for this purpose, is developed in the next section. The condition $\Delta t \leq \Delta t_{\text{crit}}$ is enforced at every increment to prevent excessively large values of the time increments resulting from a small number of activations. In practice, we found that time step regulation is only needed in the initial loading steps. After the onset of yielding, the time step tends to fluctuate around a steady-state value lower than the critical time step, as sketched in Fig. 2. A summary of the calculation steps of the numerical mesoscale model, including the time step selection procedure, is outlined in Table 1. The collection of user subroutines developed to implement the model in Abaqus is included in the SI.

Table 1: Summary of the calculation steps of the mesoscale STZ model.

1. Initialisation of the simulation

1.a Discretise domain into *n* finite elements.

1.b Define list of *n* STZs.

1.c Apply initial conditions at $t = t_0$.

2. First increment (*j* = 0, no STZ event)

2.a Compute average stress state $\bar{\boldsymbol{\sigma}}_i$ and corresponding value of $\dot{s}_i$ via Eq. (10) for each STZ.

2.b Use KMC algorithm to calculate Δt_0 via Eq. (16) and random number ξ_1. If $\Delta t_0 > \Delta t_{\text{crit}}$, $\Delta t_0 = \Delta t_{\text{crit}}$.

2.c Update simulation time: $t = t_1 = t_0 + \Delta t_0$.

2.d Compute equilibrium stresses and strains satisfying boundary conditions via the built-in FE solver**.**

3. Subsequent increments (with one STZ event per increment)

3.a Update increment counter: $j = j + 1$

3.b Compute average stress state $\bar{\boldsymbol{\sigma}}_i$ and corresponding values of $\dot{s}_i$, $\bar{\tau}_{\max,i}$, and ω_i via Eqs. (19) to (21) for each STZ.

3.c Use KMC method to calculate Δt_j via Eq. (16) and random number ξ_1. If $\Delta t_j > \Delta t_{\text{crit}}$, $\Delta t_j = \Delta t_{\text{crit}}$

3.d Use KMC method (Eq. (18)) to select STZ to distort via random number ξ_2.

3.e Update simulation time: $t = t_{j+1} = t_j + \Delta t_j$.

3.f Apply a uniform shear eigenstrain of magnitude γ_0 via Eq. (22) on the selected STZ and compute equilibrium stresses and strains satisfying boundary conditions via the built-in FE solver**.**

3.g If $t < t_{\text{end}}$, return to 3.a.

4. Terminate the simulation at $t = t_{\text{end}}$

3.4 Boundary value problem

In the remainder of the study, we consider boundary-value problems (BVPs) defined by a rectangular domain (of initial height h_0 and initial width w_0) subjected to periodic boundary conditions representative of plane strain compression. At each time step, the nominal strain in the x_2-direction is calculated based on a prescribed true macroscopic strain rate (see Figs. 1 and 2). The transverse (x_1-direction) and shear components of the macroscopic strain are determined iteratively at each time step so that the corresponding macroscopic stress components vanish. Plane strain conditions are applied in the out-of-plane x_3-direction. One node is constrained to prevent rigid body movement. All calculations shown in this paper are conducted for identical ratios of h_0/w_0 (= 2.5) and for different domain sizes ranging from n = 150 to n = 8150 elements (by changing the amount of close to equisized triangular elements along the width, n_w, from 11 to 80, respectively). Recall that the total number of elements is equal to the number of STZs. An additional set of files required to simulate the 2D plane strain compression with periodic boundary conditions is provided in the SI.

An illustration of the typical macroscopic stress-strain response under plane-strain compression applied in the x_2-direction is shown in Fig. 2. There are only a few STZ activations in the initial linear, elastic regime, see the insert for $t = t_7$. At the yield point, a sufficient number of STZ activations has taken place to generate a steady-state flowing structure, often characterised by the nucleation of shear band structures oriented at $\pm 45°$ with respect to the loading direction. The value of the time increment prescribed by the KMC algorithm fluctuates around a steady-state value Δt^* during steady-state flow. Numerical results illustrating this behaviour are analysed in detail in section 5.

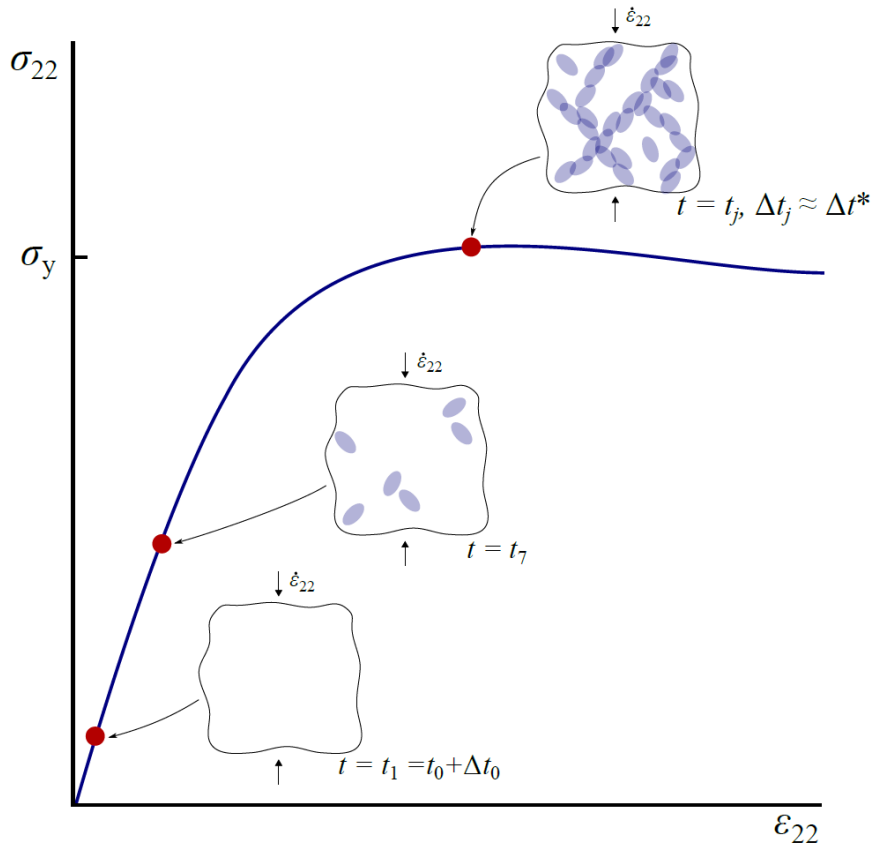

Fig. 2: Example of a typical macroscopic stress-strain response predicted by the computational STZ model of a material domain in plane strain compression ($\varepsilon_{33} = 0$) at constant macroscopic strain rate $\dot{\varepsilon}_{22}$. Additional sketches show the accumulated STZ activation events at three simulation stages: (1) after the first time increment, (2) in the linear, elastic regime where only a few STZ activations have taken place, and (3) when macroscopic yielding has occurred. Beyond this point, the value of the time increment fluctuates around a stable characteristic value Δt^*.

4. Mean-field approximation

We explore the use of a mean-field approximation to estimate the dependence of the predicted value of the yield strength by the STZ framework upon the values of the model parameters. Specifically, we aim to derive an explicit relationship between the yield strength and the (prescribed) strain rate. The approximate relationship can be used to regulate the time increment (by providing an a priori estimation for the value of σ_y for Eq. (26)) and to calibrate the framework to measured data on an amorphous material system. We limit our attention to the case of plane strain compression in this paper. However, the mean-field theory is readily adapted to any simple loading state representative for the measurement conditions.

Consider an amorphous solid in plane strain compression subjected to a constant macroscopic strain rate $\dot{\varepsilon}_{22}$. The solid is enriched with the STZ mesoscale framework detailed in sections 2 and 3. As mentioned in the previous section, the time increment calculated by the KMC algorithm fluctuates around a constant, characteristic value, Δt^*, during steady-state flow. Therefore, the macroscopic strain rate can be expressed as:

$$\dot{\varepsilon}_{22} = \frac{\Delta \varepsilon_{22}^*}{\Delta t^*}, \tag{27}$$

where $\Delta \varepsilon_{22}^*$ is a characteristic value of the plastic strain increment during flow. Following Argon (2013), the latter can be approximated by the average plastic strain due to one STZ transformation:

$$\Delta \varepsilon_{22}^* = \frac{\gamma_0}{2} \frac{n_{\mathrm{el}}}{n}, \tag{28}$$

where the ratio n_{el} / n represents the volume fraction of one STZ.

We proceed by establishing a relationship between the characteristic time step and the flow stress. Now, recall that the value of Δt is calculated via the KMC method by making use of Eq. (17)during each increment where the random number ξ_1 is evenly distributed on the]0,1] interval. Consequently, we propose the following estimate for the characteristic time step:

$$\Delta t^* = \left(n s^* \right)^{-1}, \tag{29}$$

where s^* is a characteristic attempt rate at yield based on Eq. (10):

$$\dot{s}^* = f_{\mathrm{d}} \exp\left[\frac{-v_0}{k_{\mathrm{B}}T}\left(CG\gamma_0 + 0.5\left(\hat{\tau} - 0.5c_1\sigma_{\mathrm{y}}\right)\right)\right]. \tag{30}$$

In writing Eq. (29), we made use of the fact that the expected value of the -ln(ξ_1) distribution between 0 and 1 is equal to unity. In writing (21), we have assumed that $\bar{\sigma}_{11} = \sigma_{\mathrm{y}}$ is the only non-zero, in-plane stress component of the average stress $\bar{\boldsymbol{\sigma}}$ for all STZs during yielding. To compensate for this uniaxial stress approximation, we introduce a calibration factor c_1 of magnitude close to unity. All calculations for the BVP analysed in this paper assume $c_1 = 1.14$.

Combining Eqs. (27) to (30), we obtain a relationship between the predicted yield strength σ_{y} and the selected value of the fundamental model parameters: the activation eigenstrain, γ_0, and the activation volume, v_0:

$$\sigma_{\mathrm{y}} = c_1^{-1}\left[4CG\gamma_0 + 2\hat{\tau} + \frac{4k_{\mathrm{B}}T}{v_0}\ln\left(\frac{2\dot{\varepsilon}_{22}}{n_{\mathrm{el}}\gamma_0 f_{\mathrm{d}}}\right)\right]. \tag{31}$$

5. Results and discussion

We first discuss typical STZ model predictions for the deformation response of a model metallic and model polymeric glass in plane strain compression. These reference calculations serve to illustrate the representative simulated deformation behaviour and evolution of the time increment by the model. The calculated value of the yield strength is also compared to the estimated value via the analytical mean-field approximation. In addition, we discuss the use and the effect of a bound on the value of the time increment on the deformation response. This is followed by a more detailed validation of the mean-field approximation focusing on the metallic glass material system, including a domain size sensitivity study. Some guidelines for calibration of the STZ model via the validated mean-field theory are formulated at the end the section.

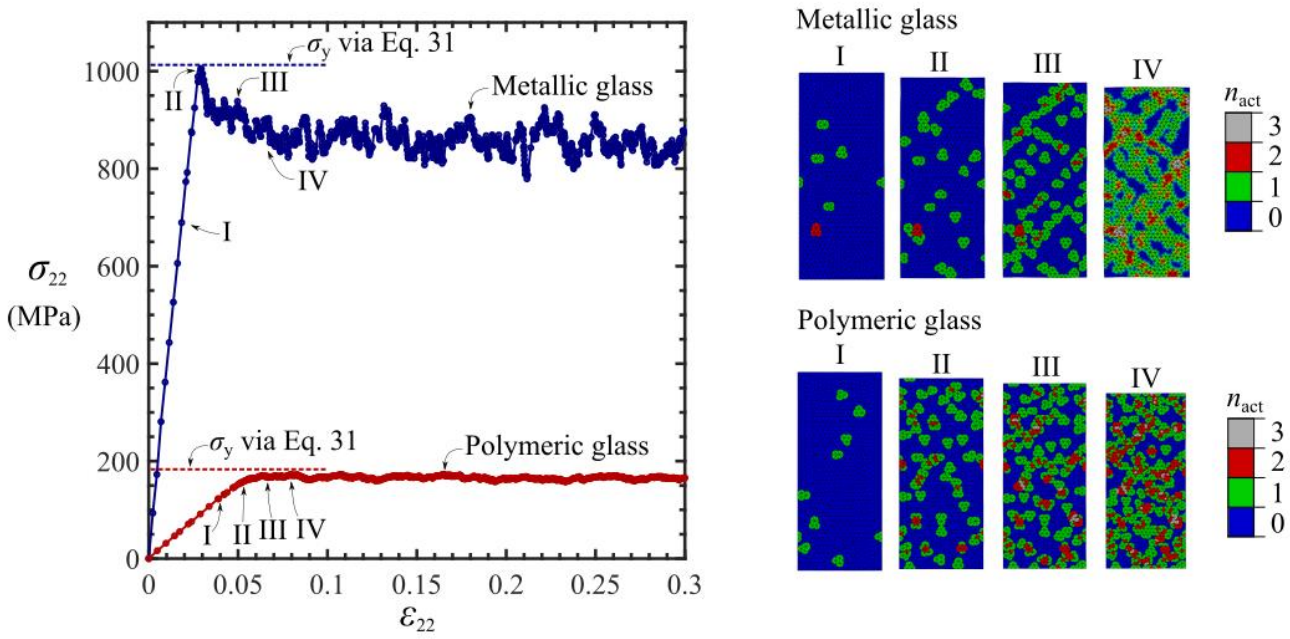

Fig. 3: Macroscopic stress-strain response in plane strain compression at T = 293 K and for $\dot{\varepsilon} = 10^{-2}$ s^{-1} for two representative materials. Model parameters for the two material systems are summarised in Table 2 (n = 2204, $\Delta t_{\text{crit}} = 0.24$ s for the metallic glass and $\Delta t_{\text{crit}} = 0.5$ s for the polymeric glass). The predicted value of the yield strength σ_y via Eq. (31) is included for the two reference calculations. Snapshots for each model material system show the number of cumulative activations, n_{act}, of each element during different stages of the simulation close to yield.

5.1 Reference calculations for metallic and polymeric glasses

Reference model predictions for the BVP defined in section 3.4 (with n = 2104) are presented for two distinct model material systems: a metallic glass metallic glass and a polymeric glass. The selected values of the model parameters for the two materials are given in Table 2. The values of the parameters for the metallic glass correspond to those selected by Schuh and co-workers (Homer et al., 2010; Homer and Schuh, 2009) to predict deformation mechanism maps of a Vitreloy 1 ($Zr_{41.2}Ti_{13.8}Cu_{12.5}Ni_{10}Be_{22.5}$) metallic glass via their STZ-based mesoscale framework. The values of the parameters for the glassy polymer are based on the work of Vu-Bac et al. (2015) and Chevalier et al. (2018) who analysed the deformation response of epoxy polymers via molecular and mesoscale modelling.

The macroscopic stress σ_{22} versus macroscopic strain ε_{22} response of the rectangular bar when deformed in compression at T = 293 K and for $\dot{\varepsilon}_{22} = 10^{-2}$ s^{-1} is shown in Fig. 3 for the metallic and the polymeric glass. The predicted stress-strain response is elastic-plastic for both materials. The yield strength (at peak force) σ_y is close to 1000 MPa for the metallic glass, which is in agreement with uniaxial compression data for Vitreloy 1 in the literature (Lu et al., 2003). The predicted value of σ_y is close to 180 MPa for the polymeric glass, which is in line with measured data for an epoxy in uniaxial compression (Morelle et al., 2017). It is emphasised that the model does not include a free volume-like model parameter, which has been used by Li et al. (2013) to capture the intrinsic post-yield softening behaviour typically observed on the measured stress-strain behaviour of metallic and polymeric glasses. Consequently, the predicted stress-strain response by our model does not exhibit a distinct drop in stress after yield when there are no well-defined shear bands acting as a softening mechanism. In addition, we do not account for strain hardening (which is typically observed on the stress-strain response of a polymeric glasses at large deformation) as we focus on predicted yield behaviour. We refer to the approach of Chevalier et al. (2018) to include strain hardening in the model analysed in this work.

The estimated value of σ_y via the mean-field approximation detailed in section 4 is also included for each material. Good agreement between the numerical and analytical results is observed for both materials. A more extensive validation of the mean-field model is provided below. Note that

there is no failure mechanism included in the framework, and the simulation is terminated at a predetermined strain value via the $t = t_{\text{end}}$ condition (see Table 1), corresponding to $\varepsilon_{22} = 0.3$.

Table 2: Model parameters for the reference calculations on a model metallic glass (corresponding to the data of Schuh and co-workers (Homer et al., 2010; Homer and Schuh, 2009) for Vitreloy 1 at T = 293 K) and on a model polymeric glass (based on data for an epoxy polymer at T = 293 K used by Vu-Bac et al. (2015) and Chevalier et al. (2018)).

Parameter	**Metallic glass**	**Polymeric glass**
Shear modulus, G (GPa)	13.24	1.12
Poisson's ratio, ν	0.352	0.34
Magnitude shear eigenstrain, γ_0	0.1	0.1
Activation volume, v_0 (m^3)	1.6×10^{-28}	5.1×10^{-28}
Threshold shear strength, $\hat{\tau}$ (MPa)	930	500

The corresponding number of activations n_{act} of each element at four simulation stages (I to IV) are also included in Fig. 3. These snapshots are close to the yield point and illustrate how the dynamics of STZ activations dictate the predicted σ_{22} - ε_{22} response. Now, consider the activation contour plots of the metallic glass. Before yield (stage I), only a few STZs are activated throughout the simulated domain and the global response is linear elastic. Distorted stress fields surrounding the activated transformation zones increase the attempt rate of neighbouring STZs to transform, and clusters of STZs are formed (stage II), from which small shear bands of width on the order of the size of the STZ nucleate and propagate in a direction close to $\pm 45°$ with respect to the loading direction (stage III). The regime between stages II and III is characterised with a small drop in load: the macroscopic stress required to grow shear bands is lower than to nucleate them (Homer, 2014). When the shear bands are fully grown along the width of the bar, they start to thicken (stage IV) and stable flow is observed. The predicted STZ activation contours of the polymeric glass are similar to those of the metallic glass in the elastic regime. Close to the yield point, there is a noticeable difference: the nucleated shear band structures (oriented $\pm 45°$ with respect to the direction of loading) at yield do not grow along the full width, but widen and/or interconnect via diffuse STZ activations. No distinct softening regime on the predicted stress-strain curve is observed due to the absence of localistion via well-defined shear bands. We will demonstrate below that the degree of localisation via shear bands (in lieu of more diffuse deformation) is sensitive to the selected combination of the values of the model parameters (γ_0 and v_0).

It is insightful to plot the time increment Δt as a function of the macroscopic strain ε_{22} for a reference simulation analysed in Fig. 3; this is shown in Fig. 4 for the model metallic glass calculation (the predicted evolution of the time increment for the model polymeric glass is similar). In the linear elastic regime, the values of the individual STZ attempt rates $\dot{s}_i$ are low and the computed value of Δt by the KMC method exceeds the value of Δt_{crit}: the applied value of Δt is equal to Δt_{crit} for those initial increments (see Table 1). With increasing number of STZ activations, the maximum value of the in-plane shear stress $\bar{\tau}_{\text{max},i}$ (and the corresponding value of the attempt rate $\dot{s}_i$) of the STZs increases. Consequently, the value of the KMC-controlled time increment decreases below Δt_{crit} close to the yield point. The moving average of the time increment, $\overline{\Delta t}$, is plotted in Fig. 4 between $\varepsilon_{22} = 0.03$ (yield) and $\varepsilon_{22} = 0.3$ (end of the simulation)

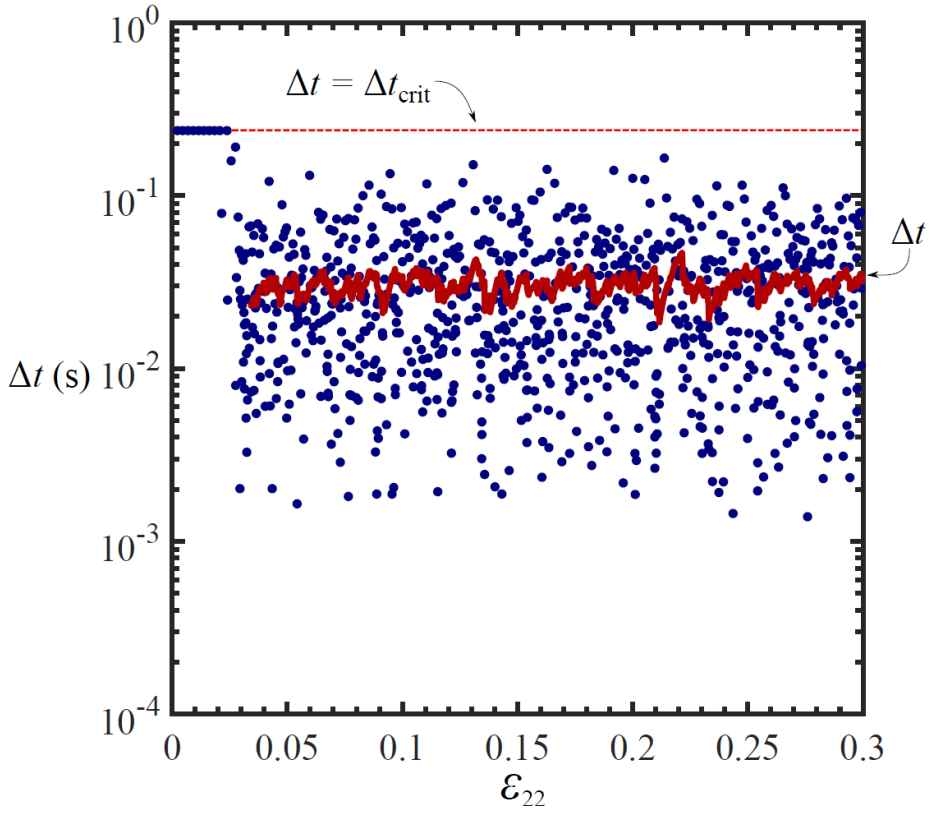

Fig. 4: Calculated value of the time increment Δt as a function of the macroscopic strain ε_{22} for the metallic glass reference calculation analysed in Fig. 3. The moving-average of the time increment, $\overline{\Delta t}$, with a 20 datapoint window size is included between $\varepsilon_{22} = 0.03$ (yield) and $\varepsilon_{22} = 0.3$ (end of the simulation).

with an averaging window of 20 increments. The computed value of $\overline{\Delta t}$ remains stable in this regime, illustrating the validity of the assumption of a close to constant value of the time increment at and beyond yield, which was used in the mean-field model.

The effect of the use of a bound of magnitude Δt_{crit} on the time increment is analysed in Fig. 5. The predicted stress-strain responses of the metallic and polymeric glass shown in Fig. 3 are included in Figs. 5a and 5b, respectively. Recall that the value of Δt_{crit} is calculated via Eq. (26) by an a priori mean-field estimation of the yield strength via Eq. (31). The calculated stress-strain response of both material systems without a bound on the time increment ($\Delta t_{\text{crit}} = \infty$) is also shown in Fig. 5. The σ_{22} - ε_{22} response for the $\Delta t_{\text{crit}} = \infty$ case in the yielding regime is clearly different from the σ_{22} - ε_{22} response computed with a bound on the time increment: the predicted value of σ_{y} is lower when there is a bound on the time increment. Note that the predicted flow strength converges to the same value for both cases. When the time increment is not bounded, the initial time increment value(s) dictated by the KMC algorithm give(s) an initial strain increment higher than the yield strain of the material, resulting in the observed artificial overshoot of the simulated material's yield strength. Now, it does not mean that a peak strength followed by softening is not possible and cannot be captured by the STZ model (see Fig. 3), but, here, the overshoot is an artifact of the KMC algorithm which must be corrected by making use of a bound on the time increment. The effect of the use of the Δt_{crit} bound is more dramatic for the polymeric glass reference simulation than for the metallic glass one. A short dicussion on the dependence of the effect of the Δt_{crit} bound on the model response upon model parameters γ_0 and v_0 is included in Appendix A. It is emphasised that the value of α to calculate Δt_{crit} via Eq. (26) is equal to 0.1 in all predictions given in this paper. In principle, the value of α can be arbitrarely chosen as long as it is lower than unity (to avoid the artificial overshoot of the yield strength) but sufficiently high to guarantee that the value of Δt_{crit} exceeds the characteristic time increment Δt^*, see Fig. 4.

5.2 Validation of the mean-field approximation

A more extensive validation of the mean-field estimation for the predicted value of the yield strength by the STZ model is now provided. Consider the map shown in Fig. 6 with axes v_0 and γ_0 and contour lines of identical yield strength via Eq. (31) for T = 293 K and $\dot{\varepsilon} = 10^{-2}$ s^{-1}. The selected values of the model parameters are listed in Table 2 for the model metallic glass (except

those of γ_0 and v_0). Selected combinations for the values of γ_0 and v_0 lie on two dashed lines on the map; one line corresponds to a constant value of γ_0 (= 0.1) and one line to a constant value of v_0 (= 5×10^{-28} m^{-3}). The predicted value of the compressive yield strength σ_y by the numerical model is plotted as a function of v_0 (for γ_0 = 0.1) and as a function of γ_0 (for v_0 = 5×10^{-28} m^{-3}) in Figs. 7a and 7b, respectively. The computed dependence of σ_y upon v_0 or γ_0 via Eq. (31) is also included. There is excellent agreement between the predicted value of σ_y by the numerical STZ framework and the value calculated via the analytical equation for low to moderate values of the eigenstrain (i.e. in the regime $0 < \gamma_0 \leq 0.2$). The mean-field approximation slightly overestimates the value of σ_y for larger values of γ_0 (i.e. $\gamma_0 > 0.2$), see Fig. 7b.

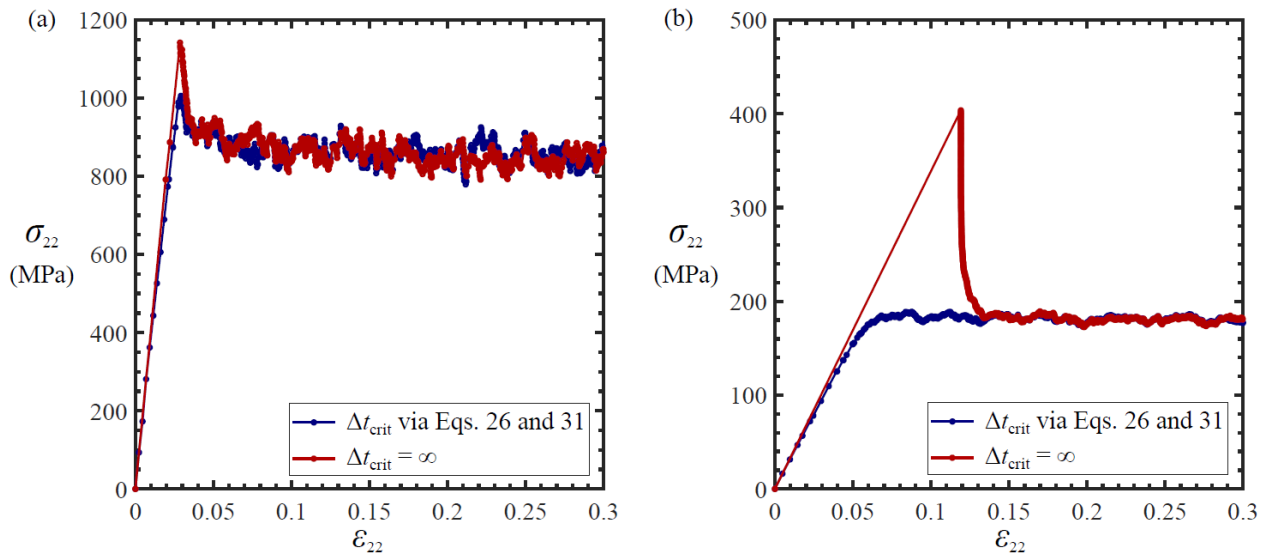

Fig. 5: Macroscopic stress-strain response of the reference calculations shown in Fig. 3 with and without the use of a bound on the value of the time increment: (a) model metallic glass and (b) model polymeric glass.

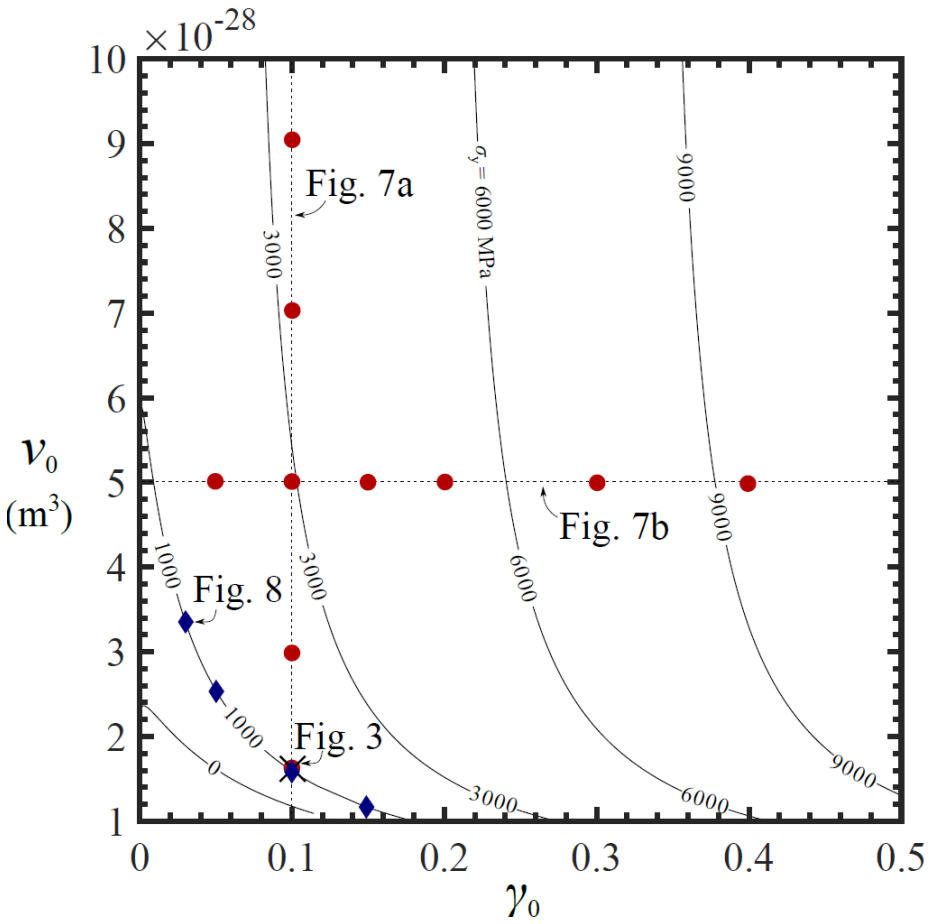

Fig. 6: Model calibration map with axes γ_0 and ν_0 and contours (solid lines) of identical yield strength σ_y via Eq. (31) for the model metallic glass analysed in Fig. 3 at T = 293 K and for $\dot{\varepsilon} = 10^{-2}$ s^{-1}; other model parameters are listed in Table 2. Locations of the selected combinations of the values of γ_0 and ν_0 explored in Figs. 3 (black cross), 7 (red dots) and 8 (blue diamonds) are included.

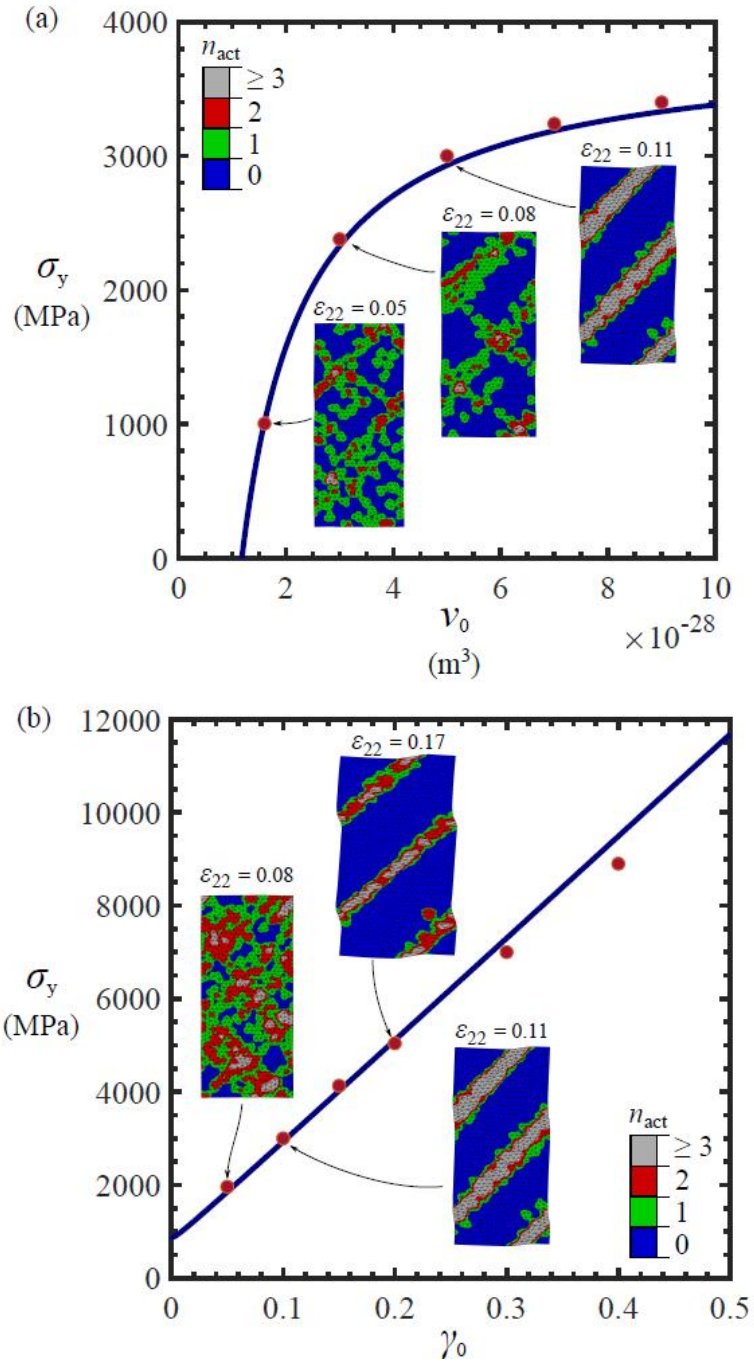

Fig. 7: Predicted value of the yield strength σ_y by the computational STZ model (dots) versus the estimated value of σ_y via Eq. (31) (solid line) for selected locations on the map shown in Fig. 6. Snapshots of the number of cumulative activations n_{act} of each element on the domain close to the material yield point ($\varepsilon_{22} = \varepsilon_y + 0.03$) are included for selected simulations.

Contour plots of the computed number of cumulative activations n_{act} of each element just after yielding (at $\varepsilon_{22} \approx \varepsilon_{\text{y}} + 0.03$) for selected simulation cases are also shown in Fig. 7. The degree of localisation of the flow at and beyond yield via well-defined shear bands is clearly dependent upon the selected combination of the values of γ_0 and ν_0. Our calculations (for both model materials) suggest that the observed degree of localisation scales with the predicted value of σ_{y}. In addition, the simulations show that the inclusion of a free volume-like state parameter (Chevalier et al., 2018; Li et al., 2013) in the framework is not required to induce severe localisation of the flow. For the metallic glass analysed in Fig. 7, the numerical results indicate that the transition from diffuse deformation (and benign softening) after yield to pronounced localisation via shear bands (with a significant drop in load) after yield occurs at a critical value of the yield strength close to 2500 MPa. It is emphasised that there is no failure or damage mechanism included in the current numerical model. In practice, it is well known that most metallic glasses exhibit close to zero ductility (when loaded in tension) due to localisation of the material flow at relatively small values of macroscopic strain (Ashby and Greer, 2006; Schuh et al., 2007) even though strategies have been developed to postpone catastrophic shear banding (Ju and Zhou, 2020; Pan et al., 2018; Xue et al., 2019).

The observed discrepancy[3] between the predicted value of σ_{y} by the mean-field theory and by the STZ framework increases with the value of γ_0 in the $\gamma_0 > 0..2$ regime, see Fig. 7b. This discrepancy is found to be insensitive to the degree of localisation. We note that atomistic simulations on metallic and polymeric glasses suggest that the value of γ_0 is typically below 0.2 (Albaret et al., 2016; Argon, 2013; Dasgupta et al., 2013; Ju and Atzmon, 2014; Mott et al., 1993; Vasoya et al., 2020) and the (theoretical) maximum value of γ_0 to prevent negative dissipation rate in the mesoscale model of Kondori et al. (2016) for an STZ-enriched solid with a (plane strain) shear

[3] We refer to the work of Bulatov and Argon (1994a), who constructed a more sophisticated analytical theory combining mean-stress and internal-stress distribution parameters to estimate the evolution of the large inelastic deformation during the simulated creep of an amorphous solid via a mesoscale STZ model. Here, we limit our attention to the estimation of the small-strain deformation behaviour of the solid (at yield) and show that even in the case of severe localisation at yield, the mean-field estimation (Eq. (31)), gives, within a reasonable regime for the value of γ_0, an acceptable estimate for the predicted yield strength by the STZ model, see Fig. 7a.

yield strength close to 1 GPa (and with selected values of the elastic constants identical to those of the metallic glass analysed in this section) is on the order of 0.1 (Vasoya et al., 2020).

5.3 Domain size dependence

We have also examined the sensitivity of the predicted deformation response by the STZ model to the domain size for different combinations of selected model parameters. This analysis differs from a standard mesh-size convergence study: the physical volume Ω ($= v_0 / \gamma_0$) associated with an STZ is dictated by the selected value of γ_0 and of v_0. Increasing the number of elements (or STZs) therefore increases the associated physical domain size.

We found the mean-field approximation to be a useful tool to analyse the convergence of the predictions as a function of domain size. For the BVP explored in this paper, the calculations converge for a sufficient number of elements along the width, n_w, the smallest dimension of the domain. As an illustration, consider the selected combinations of γ_0 and v_0 lying on the σ_y = 1000 MPa contour of the model metallic glass map shown in Fig. 6. Simulations are conducted for the selected set of model parameters, with domain sizes ranging from n = 150 (n_w = 11) to n = 8150 (n_w = 80). Recall that the length-to-width ratio (h_0/w_0 = 2.5) is identical for all calculations. The predicted value of σ_y is plotted as a function of n for the selected combinations of γ_0 and v_0 in Fig. 8a. In addition, the simulated σ_{22} - ε_{22} responses for γ_0 = 0.05 for the selected domain sizes are shown in Fig. 8b. The predicted σ_{22} - ε_{22} response (and the value of the yield strength) becomes close to domain size-independent at n = 2104 (n_w = 40). The domain size-independent value of σ_y for the cases γ_0 = 0.25 to γ_0 = 0.15 is close to the mean-field-estimated reference value of 1000 MPa.

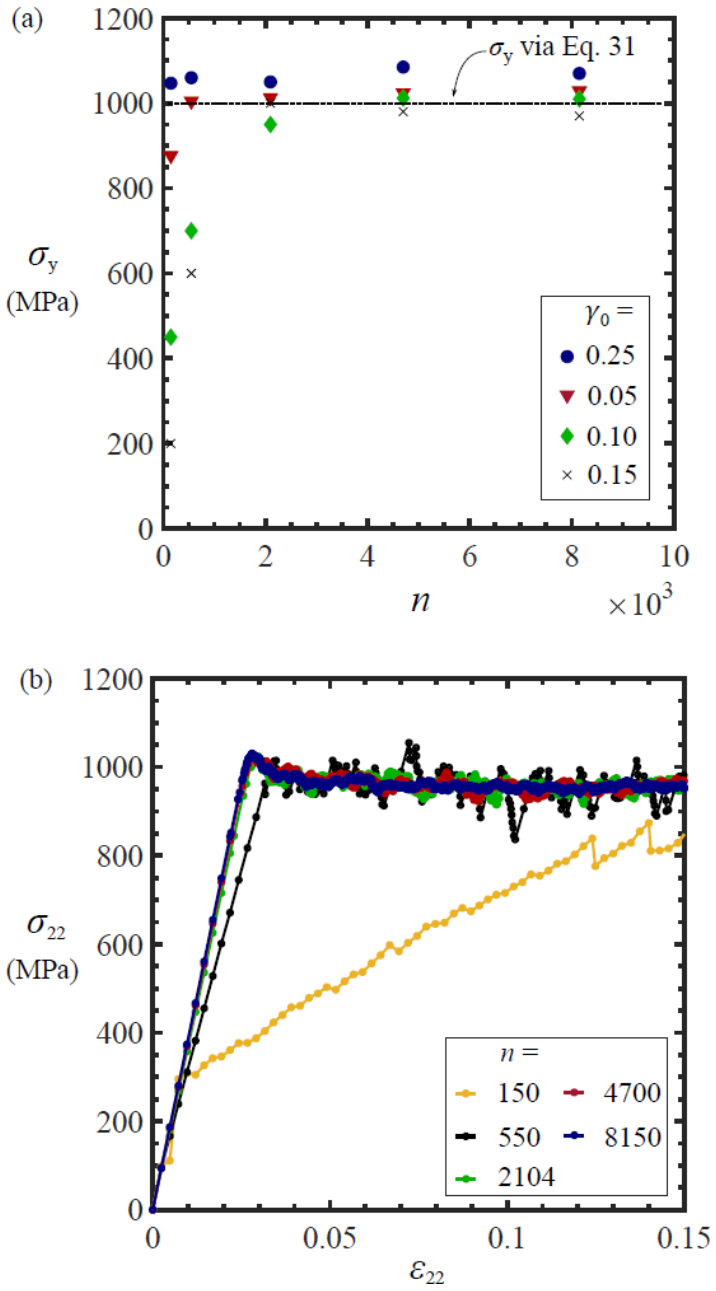

Fig. 8: (a) Calculated value of the yield strength σ_y by the computational STZ model versus the number of elements *n* discretising the simulated domain for selected combinations of the value of γ_0 and v_0 on the map shown in Fig. 6. The estimated value via the mean-field approximation is included. (b) Macroscopic stress σ_{22} versus macroscopic strain ε_{22} responses for the explored domain sizes for the case γ_0 = 0.05 and $v_0 = 2.6\times10^{-28}$ m^3.

5.4. *Parameter identification*

We conclude by exploring the use of the mean-field approximation to identify the STZ model parameters based on experimental data. In light of the present study, the idea of the STZ model calibration can be formulated as follows: given an amorphous material system of interest, what are the appropriate values of the fundamental parameters of the framework, γ_0 and v_0 needed to reproduce the reported elastic-plastic response in a similar loading scenario. The aim of the parameter identification is not to obtain a perfect fit between simulated and measured response for a particular (measurement) loading state. Instead, the essence of this discussion is to demonstrate how appropriate parametric values can be chosen based on data measured via standard tests on a solid, and to use the fitted version of the STZ model to simulate the material deformation response for more complicated loading scenarios which may be on the nano- or micro-scale. Examples of these more sophisticated simulation cases include the analysis of micro-shear band formation in a metallic glass-based composite (Hardin and Homer, 2015; Sun et al., 2016, 2018; Tong et al., 2016) or the examination of the stress-state of an epoxy matrix pocket in a fibre-reinforced composite (Pardoen et al., 2021).

To illustrate a possible parameter identification procedure via the mean-field approximation, consider the measured stress-strain response of an epoxy (RTM6) polymer (G = 1.12 and ν = 0.34) in uniaxial compression at T = 293 K at $\dot{\varepsilon} = 10^{-2}$ s^{-1} (Chevalier et al., 2018; Morelle et al., 2017), see Fig. 9a. The measured response is elastic-plastic with yield strength close to 130 MPa. A calibration map with contours of equal yield strength for T = 293 K at $\dot{\varepsilon} = 10^{-2}$ s^{-1} is constructed via the mean-field approximation, Eq. (31), see Fig. 9b. The values of the model parameters selected to draw the strength contours in Fig. 9b correspond to those listed in Table 2 (except for the values of γ_0 and v_0). The use of any combination of the values of γ_0 and v_0 on the σ_y = 130 MPa contour gives a simulated elastic-plastic response with yield strength close to 130 MPa with the numerical model. A limited amount of additional measurement data can be used to eliminate arbitrariness in the choice for the values of γ_0 and v_0. For instance, one can measure the strain rate sensitivity $\mathrm{d}\sigma_y / \mathrm{d}\ln(\dot{\varepsilon}_{22})$ of the material close to the testing temperature. The predicted value of $\mathrm{d}\sigma_y / \mathrm{d}\ln(\dot{\varepsilon}_{22})$ by the STZ framework can be matched to the measured one via the value of the activation volume v_0 by making use of the mean-field approximation:

$$v_0 = \frac{4k_{\mathrm{B}}T}{c_1}\left(\frac{\mathrm{d}\sigma_{\mathrm{y}}}{\mathrm{d}\ln(\dot{\varepsilon}_{22})}\right)^{-1}, \tag{32}$$

upon re-working Eq. (31). Morelle and co-workers (2017) measured the value of the RTM6 epoxy's activation volume ($v_0 = 5\times10^{-28}$ m^3) by a series of creep, relaxation, and strain rate jump tests at T = 293 K. Now, re-inspect the map shown in Fig. 9b. We find a fitted value of γ_0 (= 0.078) on the σ_{y} = 130 MPa contour for v_0 = 5×10^{-28} m^3. The simulated stress-strain response for γ_0 = γ_0 (= 0.078) and $v_0 = 5\times10^{-28}$ m^3 by the STZ framework (n = 2104) is plotted in Fig. 9a. There is good agreement between the measured value of the yield strength and the predicted value via the numerical model, and the structural response of the measured and calculated $\sigma_{22} - \varepsilon_{22}$ data is similar. In addition, the predicted value of yield strength via the STZ model is plotted as a function of strain rate at T = 293 K. The strain-rate sensitivity slope corresponding to $v_0 = 5\times10^{-28}$ m^3 via Eq. (32) is included; there is reasonable agreement between the input ($\mathrm{d}\sigma_y / \mathrm{d}\ln(\dot{\varepsilon}_{22})$ = 28.4 MPa for $v_0 = 5\times10^{-28}$ m^3 via Eq. (32)) and calculated ($\mathrm{d}\sigma_y / \mathrm{d}\ln(\dot{\varepsilon}_{22})$ = 30.5 MPa) value of the strain rate senstivity[4].

The parameter identifcation procedure detailed above is far from strictly rigorous; the use of the mean-field theory can be tailored to the (sometimes limited) available measured data. Likewise, it can be convenient to construct calibration maps (such as those shown in Figs. 6 and 9b), to visualise the dependence of the predicted yield strength to the values of the model parameters γ_0 and v_0 (an insightful analysis of the different regimes present on such maps is detailed in Appendix A), but these can modified based on the the available experimental data and the targeted simulation scenarios making use of the STZ model. An important related remark is that we have assumed the value of the threshold strength $\hat{\tau}$ to be known (and fixed) for a given material system. The value of

[4] Note that the reported measured value of $\mathrm{d}\sigma_y / \mathrm{d}\ln(\dot{\varepsilon}_{22})$ by Morelle and co-workers for the RMT6 epoxy is lower than 28.4 MPa as they adopted a different calculation for the activation volume compared to Eq. (32). Here, we have chosen to illustrate the calibration method by using their reported value of the activation volume, $v_0 (= 5\times10^{-28}$ m$^3)$ and demonstrate that the input value of the strain rate sensitivity to the STZ framework (corresponding to a value of v_0 via Eq. (32)) is in agreement with the predicted value of the strain sensitivity by the STZ model.

$\hat{\tau}$ should indeed be on the order of the athermal ($T = 0$) flow strength, σ_y^0, (Argon, 2013) and reads, upon modification of Eq. (31):

$$\hat{\tau} \approx \sigma_y^0 / 2 - 2CG\gamma_0 . \tag{33}$$

Atomistic and/or measurements can be used to determine a physical range for the value of σ_y^0. The choice for the value of $\hat{\tau}$ via Eq. (33) can be seen as a (limited) additional degree of freedom for the STZ model calibration.

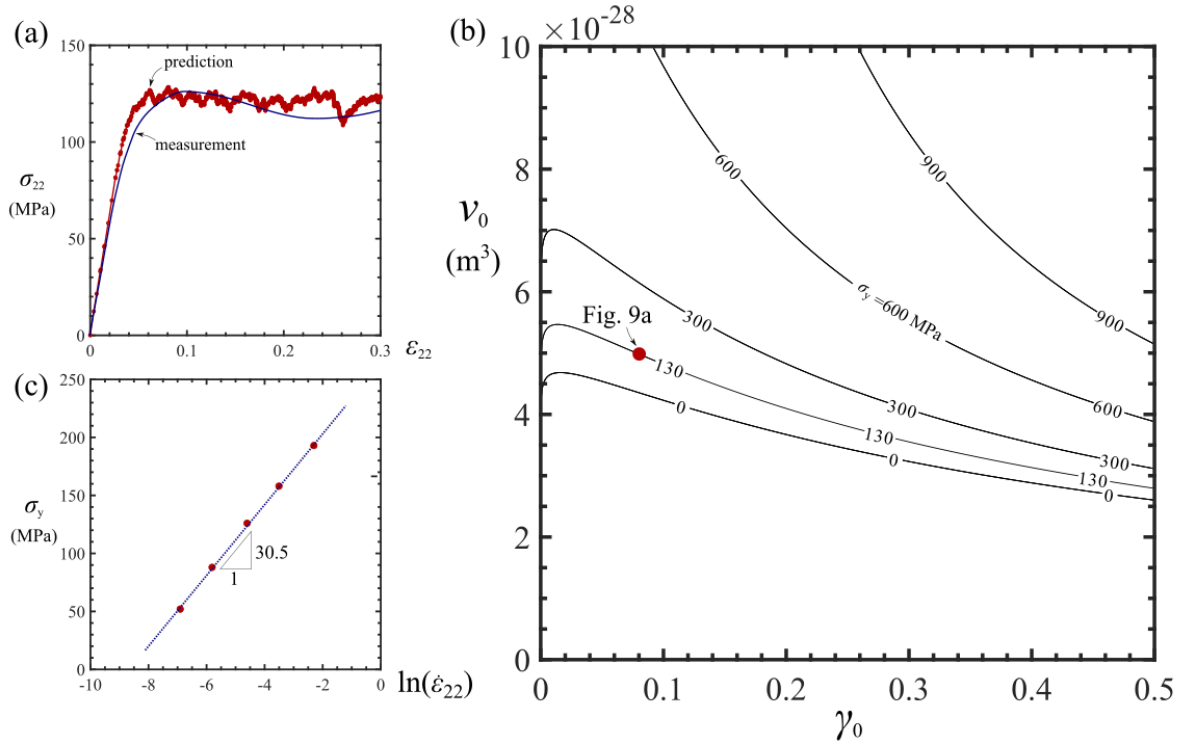

Fig. 9: Parameter identification for an RTM6 epoxy: (a) measured stress σ_{22} versus strain ε_{22} response of an RTM6 epoxy in uniaxial compression at T = 293 K and for $\dot{\varepsilon} = 10^{-2}$ s^{-1} (Chevalier et al., 2018; Morelle et al., 2017) and calculated σ_{22} - ε_{22} response by the computational plane strain model (n = 2104) with fitted values of γ_0 and v_0 highlighted in (b) for T = 293 K and $\dot{\varepsilon} = 10^{-2}$ s^{-1} (other model parameters are listed in Table 2), (b) Model calibration map for the RTM6 epoxy (G = 1.12 GPa, ν =0.34, $\hat{\tau} = 500$ MPa , T = 293 K and $\dot{\varepsilon} = 10^{-2}$ s^{-1}) with axes γ_0 and v_0 and contours of identical yield strength σ_y via Eq. (31). The location of the selected combination of values of γ_0 and v_0 for the model prediction shown in (a) is included. (c) Predicted value of the yield strength via the calibrated STZ framework as a function of imposed macroscopic strain rate. A linear fit (R^2 = 0.99) to the predicted strength data is shown via a dotted line.

6. Concluding remarks

We have implemented a mesoscale numerical model to predict the viscoplastic deformation response of amorphous materials in a finite element programme. The numerical model assumes that macroscopic plasticity of disordered solids is caused by elementary transformations of small material volumes in pure shear. The theoretical framework relies on earlier numerical implementations (Bulatov and Argon, 1994a; Chevalier et al., 2018; Homer and Schuh, 2009) of Argon's shear transformation zone (STZ) theory (Argon, 1979). Reference simulations of model metallic and polymeric glasses in plane strain compression are conducted to shed light on some fundamental issues which have received minor attention so far. The main findings of this work are:

- The dependence of the predicted yield strength by the model upon the selected values of its parameters can be estimated via a mean-field analysis. In addition, our analysis verifies that, for the selected value of the activation volume, the predicted value of the rate sensitivity by the model corresponds to the value estimated by the mean-field approximation;
- The mean-field estimation can be used to correct the kinetic Monte Carlo (KMC) time stepping scheme to prevent an unphysical predicted response at yield;
- Calibration maps are constructed to guide the parameter identification based on available measured data on an amorphous solid;

The code of the model is made available and can be the basis for several enhancements such as heterogeneous STZ properties (a preliminary illustration on this effect is included in Appendix B), the inclusion of a damage or fracture criterion to the formalism, non-isothermal loading conditions, and the presence of a viscoelastic instead of a linear elastic matrix.

Acknowledgements

Computational resources have been provided by the supercomputing facilities of the Université catholique de Louvain (CISM/UCL) and the Consortium des Équipements de Calcul Intensif en Fédération Wallonie Bruxelles (CÉCI) funded by the Fond de la Recherche Scientifique de Belgique (F.R.S.-FNRS) under convention 2.5020.11 and by the Walloon Region. Financial support from the FNRS (Grant PDR – T.0178.19) is gratefully acknowledged. The authors thank Dr. Jérémy Chevalier for the fruitful discussions and the technical assistance on the use of the code.

Supplementary material

Supplementary information includes the code (collection of Abaqus subroutines) for the model, a documentation file on the use of the code, and a set of files required to run an example plane strain compression simulation in Abaqus. The supplementary information will be available on the UC Louvain repository.

Appendix A: Regimes on an STZ model calibration map

Consider the calibration maps shown in Figs. 6 and 9b plotted via the mean-field approximation, Eq. (31). These maps can be constructed prior to conducting any time-consuming simulation to guide the STZ model parameter identification. The aim of this brief appendix is to re-examine the maps for the plane strain compression loading scenario analysed in this paper, and identify the competing regimes of the predicted deformation response present on the map. First, there is a division into a 'zero yield strength' (regime I) and an elastic-plastic (regime II) behaviour. The condition for the division between these two regimes is obtained by imposing $\sigma_y = 0$ and re-arranging Eq. (31):

$$\nu_0 = \frac{-k_B T}{CG\gamma_0 + \hat{\tau}/2} \ln\left(\frac{2\dot{\varepsilon}_{22}}{n_{el}\gamma_0 f_d}\right). \tag{A1}$$

The calibration map for the epoxy shown in Fig. 9b is re-drawn in Fig. A1; the boundary relation defined via Eq. A1 has been added to Fig. A1. An illustration of the typical predicted stress-strain response in Regime I for the plane strain compression BVP analysed in Fig. 3 is also shown in Fig. A1: the macroscopic stress in the loading direction fluctuates around zero. Simulations for combinations of values of γ_0 and ν_0 in this regime are characterised with extremely small time increments. The macroscopic stress-strain response of the amorphous solid in regime II is elastic-plastic with yield strength predicted via Eq. (31). Regime II can be subdivided into two regions. In regime IIa, the response is independent of the use of a bound on the time increment via Δt_{crit}, whereas in in regime IIb the Δt_{crit}-criterion has to be used to eliminate the artificial overshoot of the yield strength and the artificial softening response before reaching steady material flow (as shown in Fig. 5). The division between regimes IIa and IIb can be estimated by numerically solving the equation imposing the strain increment during the first time increment to be equal to the predicted yield strain:

$$\frac{\dot{\varepsilon}_{22}}{n\dot{s}_0} = \frac{\sigma_y(1-\nu)}{2G}, \tag{A2}$$

where $\dot{s}_0$ is calculated via Eq. (24) and σ_y via Eq. (31). The STZ model predicts a linear, elastic stress-strain response when simulating the plane strain compression BVP for selected values of γ_0

and v_0 in regime III. In this regime, the value of the yield strain exceeds the a priori imposed value of the strain at the end of the simulation, ε_{tot} (= $t_{\text{end}}\dot{\varepsilon}_{22}$). The boundary between regimes II and III is therefore obtained via:

$$\varepsilon_{\text{tot}} = \frac{(1-\nu)\sigma_{\text{y}}}{2G}, \tag{A3}$$

inserting Eq. (31) into Eq. A3 and re-arranging gives:

$$v_0 = \frac{2k_{\text{B}}T}{\varepsilon_{\text{tot}} G c_1 / (1-\nu) - 2CG\gamma_0 - \hat{\tau}} \ln\left(\frac{2\dot{\varepsilon}_{22}}{n_{\text{el}}\gamma f_{\text{d}}}\right) \tag{A4}$$

This criterion has also been added to Fig. A1.

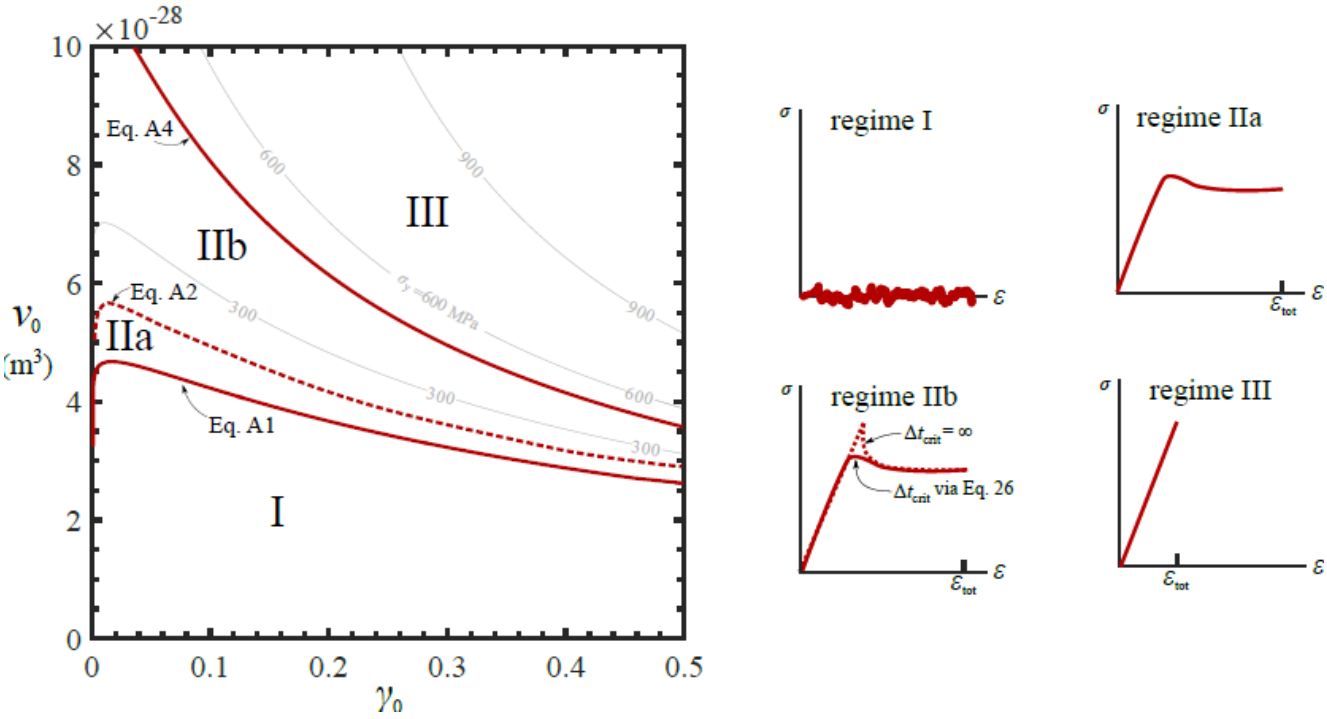

Fig. A1: Division of the map shown in Fig. 9b into regimes via Eqs. A1, A2 and A3 (for $\varepsilon_{\text{tot}} = 0.15$) and sketches of the typical homogenised stress versus strain response in the loading direction in each regime for the plane strain compression BVP analysed in this paper.

Appendix B: Effect of distribution of the eigenstrain (and activation volume)

There is strong evidence suggesting that the STZ properties (and the surrounding material stiffness) are heterogeneously distributed in an amorphous solid (Boioli et al., 2017; Tanguy, 2021; Wang et al., 2018). Atomistic calculation data indicate that transformation shear strains follow a distribution that can be approximately represented by a decaying exponential from a maximum value (Albaret et al., 2016). As a first order approximation, and similar to most existing mesoscale STZ models, we considered uniform STZ properties in this work. To explore the effect of heterogeneous STZ properties we have conducted a series of calculations with our model assuming the value of γ_0 assigned to an STZ to follow a normal distribution characterised with a mean eigenstrain $\bar{\gamma}_0$ and standard deviation S. Note that we still assume that the physical volume Ω of all STZs is uniform (this is consistent with the approximately uniform area of the STZs in our finite element model). Hence, the value of the activation volume $v_0 = (\Omega\gamma_0)$ also follows a normal distribution.

To illustrate the effect of a distribution of the value of γ_0, consider the reference σ_{22} - ε_{22} response for the model metallic glass analysed in Fig. 8b with γ_0 = 0.05, $v_0 = 2.6\times10^{-28}$ m^3 (i.e. Ω = $= 5.2\times10^{-27}$ m^3), and n = 2104, which is re-drawn in Fig. B1. The calculated σ_{22} - ε_{22} data with a normally distributed eigenstrain with mean $\bar{\gamma}_0$ = 0.05 and normalised standard deviation $S/\bar{\gamma}_0$ ranging from 0.01 to 0.1 is included in Fig. B1. The σ_{22} - ε_{22} response with a small value of $S/\bar{\gamma}_0$ (= 0.01) is almost identical to the reference response. Increasing the value of $S/\bar{\gamma}_0$ results in a decrease of value of the yield strength, and a smoother transition between the elastic part and the flow part of the σ_{22} - ε_{22} response (this is in closer agreement with the shape of measured σ_{22} - ε_{22} responses of polymeric and metallic glasses, see Fig. 9a). Our simulation data indicate that the calculated flow stress is close to insensitive to the severity of variation of γ_0 values up until $S/\bar{\gamma}_0$ $\leq$ 0.05.

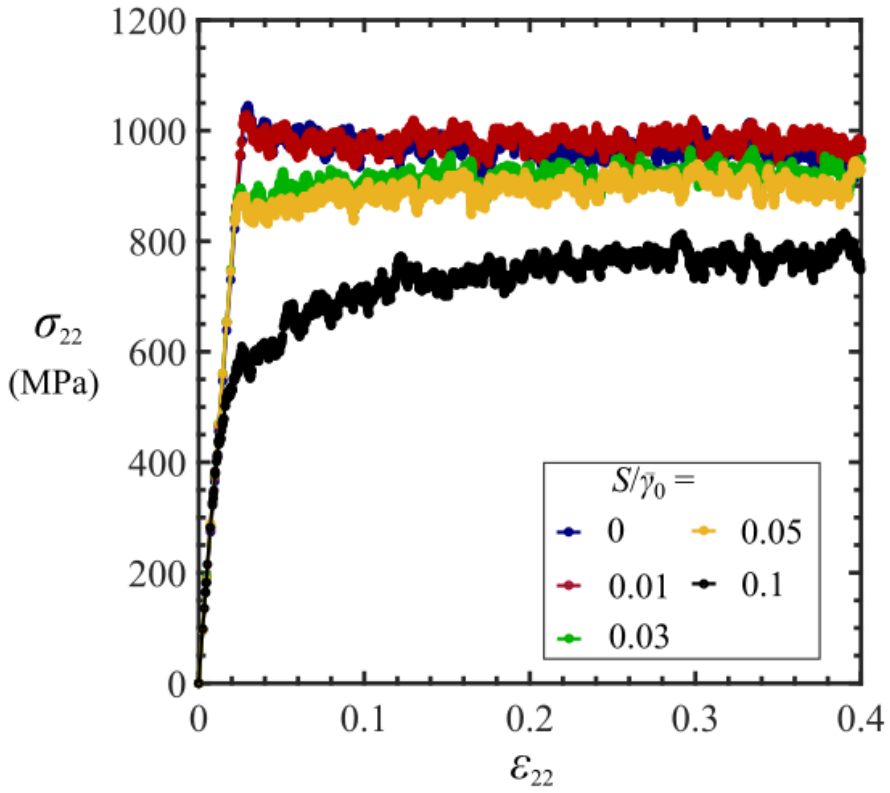

Fig. B1: Illustration of the effect of a normally distributed value of γ_0 and v_0: the σ_{22} - ε_{22} response for the model metallic glass analysed in Fig. 8b with a constant value of γ_0 (= 0.05) and $v_0 (= 2.6\times10^{-28}\ \mathrm{m}^3)$ and n = 2104 and the corresponding σ_{22} - ε_{22} data for the same material and identical testing conditions but with a normally distributed value of γ_0 assigned to each STZ (mean $\bar{\gamma}_0$ = 0.05 and normalised standard deviation $S/\bar{\gamma}_0$ ranging from 0.01 to 0.1).

References

Albaret, T., Tanguy, A., Boioli, F., Rodney, D., 2016. Mapping between atomistic simulations and Eshelby inclusions in the shear deformation of an amorphous silicon model. Phys. Rev. E 93. https://doi.org/10.1103/PhysRevE.93.053002

Ames, N.M., Srivastava, V., Chester, S.A., Anand, L., 2009. A thermo-mechanically coupled theory for large deformations of amorphous polymers. Part II: Applications. Int. J. Plast. 25, 1495–1539. https://doi.org/10.1016/j.ijplas.2008.11.005

Anand, L., Ames, N.M., Srivastava, V., Chester, S.A., 2009. A thermo-mechanically coupled theory for large deformations of amorphous polymers. Part I: Formulation. Int. J. Plast. 25, 1474–1494. https://doi.org/10.1016/j.ijplas.2008.11.004

Anand, L., Su, C., 2007. A constitutive theory for metallic glasses at high homologous temperatures. Acta Mater. https://doi.org/10.1016/j.actamat.2007.02.020

Anand, L., Su, C., 2005. A theory for amorphous viscoplastic materials undergoing finite deformations, with application to metallic glasses. J. Mech. Phys. Solids 53, 1362–1396. https://doi.org/10.1016/j.jmps.2004.12.006

Argon, A.S., 2013. The physics of deformation and fracture of polymers. Cambridge University Press. https://doi.org/10.1017/CBO9781139033046

Argon, A.S., 1979. Plastic deformation in metallic glasses. Acta Metall. 27, 47–58. https://doi.org/10.1016/0001-6160(79)90055-5

Argon, A.S., Kuo, H.Y., 1979. Plastic flow in a disordered bubble raft (an analog of a metallic glass). Mater. Sci. Eng. 39, 101–109. https://doi.org/https://doi.org/10.1016/0025-5416(79)90174-5

Argon, A.S., Shi, L.T., 1983. Development of visco-plastic deformation in metallic glasses. Acta Metall. 31, 499–507. https://doi.org/10.1016/0001-6160(83)90038-X

Argon, A.S., Shi, L.T., 1982. Analysis of plastic flow in an amorphous soap bubble raft by the use of an inter-bubble potential. Philos. Mag. A Phys. Condens. Matter, Struct. Defects Mech. Prop. 46, 275–294. https://doi.org/10.1080/01418618208239919

Ashby, M.F., Greer, A.L., 2006. Metallic glasses as structural materials. Scr. Mater. 54, 321–326. https://doi.org/10.1016/j.scriptamat.2005.09.051

Avila, K.E., Küchemann, S., Alhafez, I.A., Urbassek, H.M., 2019. Shear-transformation zone activation during loading and unloading in nanoindentation of metallic glasses. Materials (Basel). 12. https://doi.org/10.3390/ma12091477

Ayoub, G., Zaïri, F., Fréderix, C., Gloaguen, J.M., Naït-Abdelaziz, M., Seguela, R., Lefebvre, J.M., 2011. Effects of crystal content on the mechanical behaviour of polyethylene under finite strains: Experiments and constitutive modelling. Int. J. Plast. 27, 492–511. https://doi.org/10.1016/j.ijplas.2010.07.005

Baghani, M., Naghdabadi, R., Arghavani, J., Sohrabpour, S., 2012. A thermodynamically-consistent 3 D constitutive model for shape memory polymers. Int. J. Plast. 35, 13–30. https://doi.org/10.1016/j.ijplas.2012.01.007

Barriere, T., Gabrion, X., Holopainen, S., Jokinen, J., 2020. Testing and analysis of solid polymers under large monotonic and long-term cyclic deformation. Int. J. Plast. 135, 102781. https://doi.org/10.1016/j.ijplas.2020.102781

Boioli, F., Albaret, T., Rodney, D., 2017. Shear transformation distribution and activation in glasses at the atomic scale. Phys. Rev. E 95, 1–10. https://doi.org/10.1103/PhysRevE.95.033005

Bortz, A.B., Kalos, M.H., Lebowitz, J.L., 1975. A new algorithm for Monte Carlo simulation of Ising spin systems. J. Comput. Phys. 17, 10–18. https://doi.org/10.1016/0021-9991(75)90060-1

Budrikis, Z., Fernandez Castellanos, D., Sandfeld, S., Zaiser, M., Zapperi, S., 2017. Universal features of amorphous plasticity. Nat. Commun. 8:15928. https://doi.org/10.1038/ncomms15928

Budrikis, Z., Zapperi, S., 2013. Avalanche localization and crossover scaling in amorphous plasticity. Phys. Rev. E - Stat. Nonlinear, Soft Matter Phys. 88, 1–8. https://doi.org/10.1103/PhysRevE.88.062403

Bulatov, V. V., Argon, A.S., 1994a. A stochastic model for continuum elasto-plastic behavior: I.

numerical approach and strain localization. Model. Simul. Mater. Sci. Eng. 2. https://doi.org/10.1088/0965-0393/2/2/001

Bulatov, V. V., Argon, A.S., 1994b. A stochastic model for continuum elasto-plastic behavior. II. a study of the glass transition and structural relaxation. Model. Simul. Mater. Sci. Eng. 2. https://doi.org/10.1088/0965-0393/2/2/002

Bulatov, V. V., Argon, A.S., 1994c. A stochastic model for continuum elasto-plastic behavior: III. plasticity in ordered versus disordered solids. Model. Simul. Mater. Sci. Eng. 2. https://doi.org/10.1088/0965-0393/2/2/003

Chen, K.W., Lin, J.F., 2010. Investigation of the relationship between primary and secondary shear bands induced by indentation in bulk metallic glasses. Int. J. Plast. 26, 1645–1658. https://doi.org/10.1016/j.ijplas.2010.03.003

Chen, Y., Jiang, M.Q., Dai, L.H., 2013. Collective evolution dynamics of multiple shear bands in bulk metallic glasses. Int. J. Plast. 50, 18–36. https://doi.org/10.1016/j.ijplas.2013.03.010

Chen, Y., Jiang, M.Q., Dai, L.H., 2011. How does the initial free volume distribution affect shear band formation in metallic glass? Sci. China Physics, Mech. Astron. 54, 1488–1494. https://doi.org/10.1007/s11433-011-4376-z

Chevalier, J., 2018. Micromechanics of an epoxy matrix for fiber reinforced composites : experiments and physics-based modelling. PhD Thesis. UC Louvain (Belgium).

Chevalier, J., Brassart, L., Lani, F., Bailly, C., Pardoen, T., Morelle, X.P., 2018. Unveiling the nanoscale heterogeneity controlled deformation of thermosets. J. Mech. Phys. Solids 121, 432–446. https://doi.org/10.1016/j.jmps.2018.08.014

Choi, I.C., Zhao, Y., Kim, Y.J., Yoo, B.G., Suh, J.Y., Ramamurty, U., Jang, J. Il, 2012. Indentation size effect and shear transformation zone size in a bulk metallic glass in two different structural states. Acta Mater. 60, 6862–6868. https://doi.org/10.1016/j.actamat.2012.08.061

Dasgupta, R., Hentschel, H.G.E., Procaccia, I., 2013. Yield strain in shear banding amorphous solids. Phys. Rev. E - Stat. Nonlinear, Soft Matter Phys. 87, 1–14. https://doi.org/10.1103/PhysRevE.87.022810

Dassault Systèmes Simulia Corp, 2017. Abaqus.

Derlet, P.M., Maaß, R., 2021. Micro-plasticity in a fragile model binary glass. Acta Mater. 209, 116771. https://doi.org/10.1016/j.actamat.2021.116771

Derlet, P.M., Maaß, R., 2018. Thermally-activated stress relaxation in a model amorphous solid and the formation of a system-spanning shear event. Acta Mater. 143, 205–213. https://doi.org/10.1016/j.actamat.2017.10.020

Ding, J., Li, L., Wang, N., Tian, L., Asta, M., Ritchie, R.O., Egami, T., 2021. Universal nature of the saddle states of structural excitations in metallic glasses. Mater. Today Phys. 17. https://doi.org/10.1016/j.mtphys.2021.100359

Dong, J.L., Song, X., Wang, Z.J., Xiao, K.L., Liu, Y.H., Wilde, G., Wu, X.Q., Jiang, M.Q., 2021. Impact resistance of single-layer metallic glass nanofilms to high-velocity micro-particle penetration. Extrem. Mech. Lett. 44. https://doi.org/10.1016/j.eml.2021.101258

Donohue, A., Spaepen, F., Hoagland, R.G., Misra, A., 2007. Suppression of the shear band instability during plastic flow of nanometer-scale confined metallic glasses. Appl. Phys. Lett. 91. https://doi.org/10.1063/1.2821227

Eshelby, J.D., 1957. The determination of the elastic field of an ellipsoidal inclusion, and related problems. Proc. R. Soc. London. Ser. A. Math. Phys. Sci. 241, 376–396. https://doi.org/10.1098/rspa.1957.0133

Falk, M.L., Langer, J.S., 2011. Deformation and failure of amorphous, solidlike materials. Annu. Rev. Condens. Matter Phys. 2, 353–373. https://doi.org/10.1146/annurev-conmatphys-062910-140452

Federico, C.E., Bouvard, J.L., Combeaud, C., Billon, N., 2020. Modelling strain rate and temperature dependent mechanical response of PMMAs at large deformation from below to above Tg. Polymer (Guildf). 202, 122710. https://doi.org/10.1016/j.polymer.2020.122710

Felder, S., Holthusen, H., Hesseler, S., Pohlkemper, F., Gries, T., Simon, J.W., Reese, S., 2020. Incorporating crystallinity distributions into a thermo-mechanically coupled constitutive model for semi-crystalline polymers. Int. J. Plast. 135, 102751. https://doi.org/10.1016/j.ijplas.2020.102751

Fujimoto, K., Tang, Z., Shinoda, W., Okazaki, S., 2019. All-atom molecular dynamics study of impact fracture of glassy polymers. I: Molecular mechanism of brittleness of PMMA and ductility of PC. Polymer (Guildf). 178, 121570. https://doi.org/10.1016/j.polymer.2019.121570

Gan, K.F., Jiang, S.S., Huang, Y.J., Yin, H.B.C., Sun, J.F., Ngan, A.H.W., 2019. Elucidating how correlated operation of shear transformation zones leads to shear localization and fracture in metallic glasses: Tensile tests on CueZr based metallic-glass microwires, molecular dynamics simulations, and modelling. Int. J. Plast. 119, 1–20. https://doi.org/10.1016/j.ijplas.2019.02.011

Gartner, T.E., Jayaraman, A., 2019. Modeling and Simulations of Polymers: A Roadmap. Macromolecules 52, 755–786. https://doi.org/10.1021/acs.macromol.8b01836

Gillespie, D.T., 1976. A general method for numerically simulating the stochastic time evolution of coupled chemical reactions. J. Comput. Phys. 22, 403–434. https://doi.org/10.1016/0021-9991(76)90041-3

Hachour, K., Zaïri, F., Naït-Abdelaziz, M., Gloaguen, J.M., Aberkane, M., Lefebvre, J.M., 2014. Experiments and modeling of high-crystalline polyethylene yielding under different stress states. Int. J. Plast. 54, 1–18. https://doi.org/10.1016/j.ijplas.2013.06.004

Hardin, T.J., 2019. Accelerating coupled finite element-kinetic Monte Carlo models: 200 × speedup of shear transformation zone dynamics simulations. Comput. Mech. 63, 511–520. https://doi.org/10.1007/s00466-018-1606-5

Hardin, T.J., Homer, E.R., 2015. Microstructural factors of strain delocalization in model metallic glass matrix composites. Acta Mater. 83, 203–215. https://doi.org/10.1016/j.actamat.2014.09.043

Harris, M.B., Watts, L.S., Homer, E.R., 2016. Competition between shear band nucleation and propagation across rate-dependent flow transitions in a model metallic glass. Acta Mater. 111, 273–282. https://doi.org/10.1016/j.actamat.2016.03.066

Homer, E.R., 2014. Examining the initial stages of shear localization in amorphous metals. Acta Mater. 63, 44–53. https://doi.org/10.1016/j.actamat.2013.09.050

Homer, E.R., Rodney, D., Schuh, C.A., 2010. Kinetic Monte Carlo study of activated states and correlated shear-transformation-zone activity during the deformation of an amorphous metal. Phys. Rev. B - Condens. Matter Mater. Phys. 81, 1–11. https://doi.org/10.1103/PhysRevB.81.064204

Homer, E.R., Schuh, C.A., 2010. Three-dimensional shear transformation zone dynamics model for amorphous metals. Model. Simul. Mater. Sci. Eng. 18. https://doi.org/10.1088/0965-0393/18/6/065009

Homer, E.R., Schuh, C.A., 2009. Mesoscale modeling of amorphous metals by shear transformation zone dynamics. Acta Mater. 57, 2823–2833. https://doi.org/10.1016/j.actamat.2009.02.035

Hossain, D., Tschopp, M.A., Ward, D.K., Bouvard, J.L., Wang, P., Horstemeyer, M.F., 2010. Molecular dynamics simulations of deformation mechanisms of amorphous polyethylene. Polymer (Guildf). 51, 6071–6083. https://doi.org/10.1016/j.polymer.2010.10.009

Hu, Y.C., Guan, P.F., Li, M.Z., Liu, C.T., Yang, Y., Bai, H.Y., Wang, W.H., 2016. Unveiling atomic-scale features of inherent heterogeneity in metallic glass by molecular dynamics simulations. Phys. Rev. B 93, 1–7. https://doi.org/10.1103/PhysRevB.93.214202

Huang, C.C., Wei, M.K., Lee, S., 2011. Transient and steady-state nanoindentation creep of polymeric materials. Int. J. Plast. 27, 1093–1102. https://doi.org/10.1016/j.ijplas.2010.11.005

Im, S., Chen, Z., Johnson, J.M., Zhao, P., Yoo, G.H., Park, E.S., Wang, Y., Muller, D.A., Hwang, J., 2018. Direct determination of structural heterogeneity in metallic glasses using four-dimensional scanning transmission electron microscopy. Ultramicroscopy 195, 189–193. https://doi.org/10.1016/j.ultramic.2018.09.005

Jafary-Zadeh, M., Tavakoli, R., Srolovitz, D.J., Zhang, Y.W., 2016. Thermally induced failure mechanism transition and its correlation with short-range order evolution in metallic glasses. Extrem. Mech. Lett. 9, 215–225. https://doi.org/10.1016/j.eml.2016.07.009

Jang, D., Gross, C.T., Greer, J.R., 2011. Effects of size on the strength and deformation mechanism in Zr-based metallic glasses. Int. J. Plast. 27, 858–867.

https://doi.org/10.1016/j.ijplas.2010.09.010

Jatin, Sudarkodi, V., Basu, S., 2014. Investigations into the origins of plastic flow and strain hardening in amorphous glassy polymers. Int. J. Plast. 56, 139–155. https://doi.org/10.1016/j.ijplas.2013.11.007

Jensen, K.E., Weitz, D.A., Spaepen, F., 2014. Local shear transformations in deformed and quiescent hard-sphere colloidal glasses. Phys. Rev. E - Stat. Nonlinear, Soft Matter Phys. 90, 042305. https://doi.org/10.1103/PhysRevE.90.042305

Jiang, S., Huang, Y., Xue, P., Du, Q., Ru, W., Guo, S., He, C., Ning, Z., Sun, J., 2021. Determining deformation behaviors in a CuZr-based bulk metallic glass composite. J. Non. Cryst. Solids 561, 120768. https://doi.org/10.1016/j.jnoncrysol.2021.120768

Johnsen, J., Clausen, A.H., Grytten, F., Benallal, A., Hopperstad, O.S., 2019. A thermo-elasto-viscoplastic constitutive model for polymers. J. Mech. Phys. Solids 124, 681–701. https://doi.org/10.1016/j.jmps.2018.11.018

Ju, J.D., Atzmon, M., 2014. A comprehensive atomistic analysis of the experimental dynamic-mechanical response of a metallic glass. Acta Mater. 74, 183–188. https://doi.org/10.1016/j.actamat.2014.04.012

Ju, T., Zhou, H., 2020. Pressure-induced maximum shear strength and transition from shear banding to uniform plasticity in metallic glass. Extrem. Mech. Lett. 41, 101058. https://doi.org/10.1016/j.eml.2020.101058

Khan, F., Yeakle, C., 2011. Experimental investigation and modeling of non-monotonic creep behavior in polymers. Int. J. Plast. 27, 512–521. https://doi.org/10.1016/j.ijplas.2010.06.007

Kocks, U.F., Argon, A.S., Ashby, M.F., 1975. Thermodynamics and kinetics of solids. Prog. Mater. Sci. Vol. 19. https://doi.org/10.1016/b978-0-408-01374-1.50020-8

Kondori, B., Amine Benzerga, A., Needleman, A., 2018. Discrete shear-transformation-zone plasticity modeling of notched bars. J. Mech. Phys. Solids 111, 18–42. https://doi.org/10.1016/j.jmps.2017.10.010

Kondori, B., Benzerga, A.A., Needleman, A., 2016. Discrete shear transformation zone plasticity.

Extrem. Mech. Lett. 9, 21–29. https://doi.org/10.1016/j.eml.2016.04.007

Kosiba, K., Şopu, D., Scudino, S., Zhang, L., Bednarcik, J., Pauly, S., 2019. Modulating heterogeneity and plasticity in bulk metallic glasses: Role of interfaces on shear banding. Int. J. Plast. 119, 156–170. https://doi.org/10.1016/j.ijplas.2019.03.007

Krairi, A., Doghri, I., 2014. A thermodynamically-based constitutive model for thermoplastic polymers coupling viscoelasticity, viscoplasticity and ductile damage. Int. J. Plast. 60, 163–181. https://doi.org/10.1016/j.ijplas.2014.04.010

Krairi, A., Doghri, I., Schalnat, J., Robert, G., Van Paepegem, W., 2019. Thermo-mechanical coupling of a viscoelastic-viscoplastic model for thermoplastic polymers: Thermodynamical derivation and experimental assessment. Int. J. Plast. 115, 154–177. https://doi.org/10.1016/j.ijplas.2018.11.016

Li, L., Homer, E.R., Schuh, C.A., 2013. Shear transformation zone dynamics model for metallic glasses incorporating free volume as a state variable. Acta Mater. 61, 3347–3359. https://doi.org/10.1016/j.actamat.2013.02.024

Lopes Fernandes, R., Teixeira de Freitas, S., Budzik, M.K., Poulis, J.A., Benedictus, R., 2019. From thin to extra-thick adhesive layer thicknesses: Fracture of bonded joints under mode I loading conditions. Eng. Fract. Mech. 218, 106607. https://doi.org/10.1016/j.engfracmech.2019.106607

Lu, J., Ravichandran, G., Johnson, W.L., 2003. Deformation behavior of the Zr41.2Ti13.8Cu12.5Ni10Be22.5 bulk metallic glass over a wide range of strain-rates and temperatures. Acta Mater. 51, 3429–3443. https://doi.org/10.1016/S1359-6454(03)00164-2

Lu, Y.Z., Jiang, M.Q., Lu, X., Qin, Z.X., Huang, Y.J., Shen, J., 2018. Dilatancy of shear transformations in a colloidal glass. Phys. Rev. Appl. 9. https://doi.org/10.1103/PhysRevApplied.9.014023

Malekmotiei, L., Samadi-Dooki, A., Voyiadjis, G.Z., 2015. Nanoindentation Study of Yielding and Plasticity of Poly(methyl methacrylate). Macromolecules 48, 5348–5357. https://doi.org/10.1021/acs.macromol.5b01064

Martinet, C., Heili, M., Martinez, V., Kermouche, G., Molnar, G., Shcheblanov, N., Barthel, E.,

Tanguy, A., 2020. Highlighting the impact of shear strain on the SiO2 glass structure: From experiments to atomistic simulations. J. Non. Cryst. Solids 533, 119898. https://doi.org/10.1016/j.jnoncrysol.2020.119898

Morelle, X.P., Chevalier, J., Bailly, C., Pardoen, T., Lani, F., 2017. Mechanical characterization and modeling of the deformation and failure of the highly crosslinked RTM6 epoxy resin. Mech. Time-Dependent Mater. 21, 419–454. https://doi.org/10.1007/s11043-016-9336-6

Mott, P.H., Argon, A.S., Suter, U.W., 1993. Atomistic modelling of cavitation of glassy polymers. Philos. Mag. A Phys. Condens. Matter, Struct. Defects Mech. Prop. 68, 537–564. https://doi.org/10.1080/01418619308213980

Narayan, S., Anand, L., 2021. Fracture of amorphous polymers: A gradient-damage theory. J. Mech. Phys. Solids 146, 104164. https://doi.org/10.1016/j.jmps.2020.104164

Packard, C.E., Homer, E.R., Al-Aqeeli, N., Schuh, C.A., 2010. Cyclic hardening of metallic glasses under hertzian contacts: Experiments and STZ dynamics simulations. Philos. Mag. 90, 1373–1390. https://doi.org/10.1080/14786430903352664

Pan, D., Inoue, A., Sakurai, T., Chen, M.W., 2008. Experimental characterization of shear transformation zones for plastic flow of bulk metallic glasses. Proc. Natl. Acad. Sci. U. S. A. 105, 14769–14772. https://doi.org/10.1073/pnas.0806051105

Pan, J., Chen, Q., Liu, L., Li, Y., 2011. Softening and dilatation in a single shear band. Acta Mater. 59, 5146–5158. https://doi.org/10.1016/j.actamat.2011.04.047

Pan, J., Wang, Y.X., Guo, Q., Zhang, D., Greer, A.L., Li, Y., 2018. Extreme rejuvenation and softening in a bulk metallic glass. Nat. Commun. 9. https://doi.org/10.1038/s41467-018-02943-4

Pardoen, T., Ferracin, T., Landis, C.M., Delannay, F., 2005. Constraint effects in adhesive joint fracture. J. Mech. Phys. Solids 53, 1951–1983. https://doi.org/10.1016/j.jmps.2005.04.009

Pardoen, T., Klavzer, N., Gayot, S., Van Loock, F., Chevalier, J., Morelle, X., Destoop, V., Lani, F., Camanho, P., Brassart, L., Nysten, B., Bailly, C., 2021. Nanomechanics serving polymer-based composite research. Comptes Rendus. Phys. 22, 1–22. https://doi.org/10.5802/crphys.56

Park, H., Choi, J., Kim, B., Yang, S., Shin, H., Cho, M., 2018. Toward the constitutive modeling of epoxy matrix: Temperature-accelerated quasi-static molecular simulations consistent with the experimental test. Compos. Part B Eng. 142, 131–141. https://doi.org/10.1016/j.compositesb.2018.01.018

Perepezko, J.H., Imhoff, S.D., Chen, M.W., Wang, J.Q., Gonzalez, S., 2014. Nucleation of shear bands in amorphous alloys. Proc. Natl. Acad. Sci. U. S. A. 111, 3938–3942. https://doi.org/10.1073/pnas.1321518111

Phan, T., Rigelesaiyin, J., Chen, Y., Bastawros, A., Xiong, L., 2020. Metallic glass instability induced by the continuous dislocation absorption at an amorphous/crystalline interface. Acta Mater. 189, 10–24. https://doi.org/10.1016/j.actamat.2020.02.038

Regrain, C., Laiarinandrasana, L., Toillon, S., Saï, K., 2009. Multi-mechanism models for semi-crystalline polymer: Constitutive relations and finite element implementation. Int. J. Plast. 25, 1253–1279. https://doi.org/10.1016/j.ijplas.2008.09.010

Richard, D., Ozawa, M., Patinet, S., Stanifer, E., Shang, B., Ridout, S.A., Xu, B., Zhang, G., Morse, P.K., Barrat, J.L., Berthier, L., Falk, M.L., Guan, P., Liu, A.J., Martens, K., Sastry, S., Vandembroucq, D., Lerner, E., Manning, M.L., 2020. Predicting plasticity in disordered solids from structural indicators. Phys. Rev. Mater. 4, 1–19. https://doi.org/10.1103/PhysRevMaterials.4.113609

Rozanski, A., Galeski, A., 2013. Plastic yielding of semicrystalline polymers affected by amorphous phase. Int. J. Plast. 41, 14–29. https://doi.org/10.1016/j.ijplas.2012.07.008

Sandfeld, S., Budrikis, Z., Zapperi, S., Castellanos, D.F., 2015. Avalanches, loading and finite size effects in 2D amorphous plasticity: Results from a finite element model. J. Stat. Mech. Theory Exp. 2. https://doi.org/10.1088/1742-5468/2015/02/P02011

Schuh, C.A., Hufnagel, T.C., Ramamurty, U., 2007. Mechanical behavior of amorphous alloys. Acta Mater. 55, 4067–4109. https://doi.org/10.1016/j.actamat.2007.01.052

Shojaei, A., Guoqiang L., 2014. Thermomechanical constitutive modelling of shape memory polymer including continuum functional and mechanical damage effects. Proc. R. Soc. A Math. Phys. Eng. Sci. 470.

Shojaei, A.K., Volgers, P., 2017. Fatigue damage assessment of unfilled polymers including self-heating effects. Int. J. Fatigue 100, 367–376. https://doi.org/10.1016/j.ijfatigue.2017.03.017

Srivastava, V., Chester, S.A., Ames, N.M., Anand, L., 2010. A thermo-mechanically-coupled large-deformation theory for amorphous polymers in a temperature range which spans their glass transition. Int. J. Plast. 26, 1138–1182. https://doi.org/10.1016/j.ijplas.2010.01.004

Sun, B.A., Song, K.K., Pauly, S., Gargarella, P., Yi, J., Wang, G., Liu, C.T., Eckert, J., Yang, Y., 2016. Transformation-mediated plasticity in CuZr based metallic glass composites: A quantitative mechanistic understanding. Int. J. Plast. 85, 34–51. https://doi.org/10.1016/j.ijplas.2016.06.004

Sun, H.C., Ning, Z.L., Wang, G., Liang, W.Z., Pauly, S., Huang, Y.J., Guo, S., Xue, X., Sun, J.F., 2018. In-situ tensile testing of ZrCu-based metallic glass composites. Sci. Rep. 8, 1–12. https://doi.org/10.1038/s41598-018-22925-2

Sundararaghavan, V., Kumar, A., 2013. Molecular dynamics simulations of compressive yielding in cross-linked epoxies in the context of Argon theory. Int. J. Plast. 47, 111–125. https://doi.org/10.1016/j.ijplas.2013.01.004

Tanguy, A., 2021. Elasto-plastic behavior of amorphous materials: a brief review. Comptes Rendus Phys. 22, 1–17.

Tong, X., Wang, G., Yi, J., Ren, J.L., Pauly, S., Gao, Y.L., Zhai, Q.J., Mattern, N., Dahmen, K.A., Liaw, P.K., Eckert, J., 2016. Shear avalanches in plastic deformation of a metallic glass composite. Int. J. Plast. 77, 141–155. https://doi.org/10.1016/j.ijplas.2015.10.006

Urata, S., Li, S., 2018. A multiscale shear-transformation-zone (STZ) model and simulation of plasticity in amorphous solids. Acta Mater. 155, 153–165. https://doi.org/10.1016/j.actamat.2018.05.058

Van Loock, F., Thouless, M.D., Fleck, N.A., 2019. Tensile fracture of an adhesive joint: the role of crack length and of material mismatch. J. Mech. Phys. Solids 130, 330–348. https://doi.org/10.1016/j.jmps.2019.06.004

Vasoya, M., Benzerga, A.A., Needleman, A., 2021. Shear Transformation Zone (STZ) plasticity analysis of constrained shear. Mech. Mater. 160, 103935.

https://doi.org/10.1016/j.mechmat.2021.103935

Vasoya, M., Kondori, B., Benzerga, A.A., Needleman, A., 2020. Energy dissipation rate and kinetic relations for Eshelby transformations. J. Mech. Phys. Solids 136, 103699. https://doi.org/10.1016/j.jmps.2019.103699

Vasoya, M., Kondori, B., Benzerga, A.A., Needleman, A., 2019. Limits on transformation strains for non-negative dissipation. J. Appl. Mech. Trans. ASME 86, 1–7. https://doi.org/10.1115/1.4042577

Voyiadjis, G.Z., Malekmotiei, L., Samadi-Dooki, A., 2018. Indentation size effect in amorphous polymers based on shear transformation mediated plasticity. Polymer (Guildf). 137, 72–81. https://doi.org/10.1016/j.polymer.2018.01.006

Voyiadjis, G.Z., Samadi-Dooki, A., 2016. Constitutive modeling of large inelastic deformation of amorphous polymers: Free volume and shear transformation zone dynamics. J. Appl. Phys. 119. https://doi.org/10.1063/1.4953355

Voyiadjis, G.Z., Shojaei, A., Mozaffari, N., 2014. Strain gradient plasticity for amorphous and crystalline polymers with application to micro- and nano-scale deformation analysis. Polymer (Guildf). 55, 4182–4198. https://doi.org/10.1016/j.polymer.2014.06.015

Vu-Bac, N., Bessa, M.A., Rabczuk, T., Liu, W.K., 2015. A multiscale model for the quasi-static thermo-plastic behavior of highly cross-linked glassy polymers. Macromolecules 48, 6713–6723. https://doi.org/10.1021/acs.macromol.5b01236

Wang, J., Peng, L.F., Deng, Y.J., Lai, X.M., Fu, M.W., Ni, J., 2019. A finite strain thermodynamically-based constitutive modeling and analysis of viscoelastic-viscoplastic deformation behavior of glassy polymers. Int. J. Plast. 122, 135–163. https://doi.org/10.1016/j.ijplas.2019.06.013

Wang, N., Ding, J., Yan, F., Asta, M., Ritchie, R.O., Li, L., 2018. Spatial correlation of elastic heterogeneity tunes the deformation behavior of metallic glasses. npj Comput. Mater. 4. https://doi.org/10.1038/s41524-018-0077-8

Wang, Y.Q., Zhang, J.Y., Liang, X.Q., Wu, K., Liu, G., Sun, J., 2015. Size- and constituent-dependent deformation mechanisms and strain rate sensitivity in nanolaminated crystalline

Cu/amorphous Cu-Zr films. Acta Mater. 95, 132–144. https://doi.org/10.1016/j.actamat.2015.05.007

Wu, Y., Bei, H., Wang, Y.L., Lu, Z.P., George, E.P., Gao, Y.F., 2015. Deformation-induced spatiotemporal fluctuation, evolution and localization of strain fields in a bulk metallic glass. Int. J. Plast. 71, 136–145. https://doi.org/10.1016/j.ijplas.2015.05.006

Xu, B., Falk, M.L., Li, J.F., Kong, L.T., 2018. Predicting shear transformation events in metallic glasses. Phys. Rev. Lett. 120, 1–5. https://doi.org/10.1103/PhysRevLett.120.125503

Xue, P., Pauly, S., Gan, W., Jiang, S., Fan, H., Ning, Z., Huang, Y., Sun, J., 2019. Enhanced tensile plasticity of a CuZr-based bulk metallic glass composite induced by ion irradiation. J. Mater. Sci. Technol. 35, 2221–2226. https://doi.org/10.1016/j.jmst.2019.06.003

Yoo, B.G., Kim, J.Y., Kim, Y.J., Choi, I.C., Shim, S., Tsui, T.Y., Bei, H., Ramamurty, U., Jang, J. Il, 2012. Increased time-dependent room temperature plasticity in metallic glass nanopillars and its size-dependency. Int. J. Plast. 37, 108–118. https://doi.org/10.1016/j.ijplas.2012.04.005

Zhao, P., Li, J., Wang, Y., 2013. Heterogeneously randomized STZ model of metallic glasses: Softening and extreme value statistics during deformation. Int. J. Plast. 40, 1–22. https://doi.org/10.1016/j.ijplas.2012.06.007

Zhao, Y., Zhang, J., Wang, Y.Q., Wu, S., Liang, X., Wu, K., Liu, G., Sun, J., 2021. The metastable constituent effects on size-dependent deformation behavior of nanolaminated micropillars: Cu/FeCoCrNi vs Cu/CuZr. J. Mater. Sci. Technol. 68, 16–29. https://doi.org/10.1016/j.jmst.2020.06.042

Zhong, C., Zhang, H., Cao, Q.P., Wang, X.D., Zhang, D.X., Ramamurty, U., Jiang, J.Z., 2016a. Deformation behavior of metallic glasses with shear band like atomic structure: A molecular dynamics study. Sci. Rep. 6, 30935. https://doi.org/10.1038/srep30935

Zhong, C., Zhang, H., Cao, Q.P., Wang, X.D., Zhang, D.X., Ramamurty, U., Jiang, J.Z., 2016b. Size distribution of shear transformation zones and their evolution towards the formation of shear bands in metallic glasses. J. Non. Cryst. Solids 445–446, 61–68. https://doi.org/10.1016/j.jnoncrysol.2016.05.002

Zhou, H., Qu, S., Yang, W., 2013. An atomistic investigation of structural evolution in metallic glass matrix composites. Int. J. Plast. 44, 147–160. https://doi.org/10.1016/j.ijplas.2013.01.002